The Effects of Differential Rotation on the Spectral Energy Distribution and Line Profiles for Models of the Rapidly Rotating Star α Oph

by

Diego Castañeda

A Thesis Submitted to Saint Mary's University, Halifax, Nova Scotia in Partial Fulfillment
of the Requirements for the Degree of Master of Science in Astronomy
(Department of Astronomy and Physics)

December 18, 2012, Halifax, Nova Scotia

Approved:_____
Dr. Robert Deupree
Supervisor

Approved:_____
Dr. Ian Short
Examiner

Approved:_____
Dr. Philip Bennett
Examiner

Date: December 18, 2012.

Acknowledgements

First, I would like to thank my supervisor, Dr. Robert Deupree for giving me the opportunity to work with him over the last two years; it has been a great experience. His guidance, patience and wisdom propelled this work forward, and there still are some great things to come. I would also like to thank Dr. Ian Short for all his help with PHOENIX and modelling atmospheres, a key component our calculations. I would also like to thank Drs. Ian Short and Phillip Bennet for being part of my defense committee.

I especially would like to thank Compute Canada (ACEnet), the Canada Foundation for Innovation (CFI), the Nova Scotia Research Innovation Trust (NSRIT), and Saint Mary's University for providing all the computational tools necessary to complete this work.

Thanks to my family for all the help and cheering up from far away. I also appreciate all the good times and discussions with my fellow graduate students, Liz, Jason, Patrick, Michael, Mitch, Kirsten, Sherry and James. Finally, special thanks to Anneya, TPT and Lambert for sitting with me for many hours while working on this document, providing me with help, laughs and stories that kept me moving forward.

Contents

List of Figures

List of Tables

Abstract

The Effects of Differential Rotation on the Spectral Energy

Distribution and Line Profiles for Models of the Rapidly Rotating

Star α Oph

by Diego Castañeda

The spectrum of the rapidly rotating star α Oph was modeled to examine the effect differential rotation has on its observed SED. Rotating stellar structure models were generated using the code ROTORC and constrained by the star's interferometrically inferred parameters. The integrator code CLIC was used to calculate the SED of each model with an NLTE atmosphere (generated by the PHOENIX code) as it would be viewed at the inclination of α Oph. Comparison of the resultant synthetic SEDs and observations of the star revealed little difference between the goodness of fits of models with different rotation profiles due to the star's inclination. Higher quality observations are necessary to further constrain the physical parameters and angular momentum distribution of α Oph but other previously observed rapidly rotating stars are current candidates for study with this technique.

December 18, 2012

Chapter 1

Introduction

1.1 Background

Significant advances in the understanding of stellar interiors and evolution have been made in the last century by increasingly refined observations and by the increase in available computational resources to solve numerically the equations that describe the physics inside stars. Most of this research, however, has focused on spherical stars. The most common case of nonspherical stars is rapidly rotating stars with sufficiently large centrifugal forces to distort considerably the surface of the star. Sufficiently large rotation generates hydrodynamic and thermal instabilities in the interior of the star that may change its composition and rotation profiles and hence change a star's properties and evolution. Rapid rotation can change considerably the physically relevant properties of a star deduced from the colors and line profiles observed. HR diagrams, masses, lifetimes and other deduced parameters derived from the assumption of spherical symmetry (implying isotropic flux

coming out of the star) need to be revised to include the angle dependence at which the star is being observed.

In order to detect if a star is rotating and how fast if so, one must analyze its individual spectral lines. The line profiles will be broadened by the Doppler effect as parts of the surface move towards or away from the observer with respect to the center of mass of the star. A comparison between this line profile and an unbroadened one will reveal the rotation rate at which we observe the star rotating. One must be careful to take into account that this velocity observed depends on the inclination (i) with respect to the axis of rotation at which the star is being observed ($i = 0°$ represents the pole-on view and $i = 90°$ represents the equator-on view), which is unknown and cannot be easily deduced from the line profile; this observed velocity is then usually expressed as $v \sin i$. It is known that early type stars are often fast rotators with values of $v \sin i$ as high $400\,\mathrm{km\,s^{-1}}$ (Abt et al. 2002). This is a significant fraction of critical rotation, at which the surface equatorial velocity is such that the centrifugal force equals with the gravitational force. One particular problem for very rapidly rotating stars is that the lines become so broad and shallow that it becomes very difficult to distinguish the presence of a line at all, as can be understood by recognizing that rotation does not change the equivalent width of the line.

Another important factor that will modify the line profile is the angular momentum distribution on the visible surface of the star. Most early studies considered only solid body rotation (Ostriker & Mark 1968; Faulkner et al. 1968; Kippenhahn et al. 1970), but there is currently a fairly high interest in differential rotation (Jackson et al. 2004; Lovekin 2005). While differential rotation refers to any non constant rotation profile, we will be

most interested here in a regime in which the angular velocity varies with distance from the rotation axis. (Gillich 2007) searched for consequences of these different rotation profiles in the stellar spectrum, both in the broad band spectral energy distribution (SED) and in the individual line profiles. There are noticeable differences when significant differential rotation is compared to the solid body case but determining which law describes better what is observed from a rotating star will depend greatly on the quality of the observations made for the star in question.

Over the last decade important advances towards improving our knowledge of the internal structure of rotating stars have been made by combining new interferometric observations and asteroseismic studies of some known fast rotators. Interferometry has improved to a point in which it is possible to resolve the deformed stellar disk of a star deformed by rapid rotation (van Belle et al. 2001, Domiciano de Souza et al. 2003, Aufdenberg et al. 2006, McAlister et al. 2005, Zhao et al. 2009). These studies have constrained important surface parameters like the value the effective temperature and the surface radius at the pole and at the equator. Finding the actual inclination angle at which the star is being observed is also possible with high precision ($| \Delta i | \approx 1°$). For rotating stars two useful quantities can give insight on how fast is a star rotating: the radius ratio between the pole and the equator, R_{pole}/R_{eq}, and the difference between the temperature at the pole and temperature at the equator, $T_{pole} - T_{eq}$. Regulus, a rapidly rotating star relatively close to critical rotation and thought to be rotating at about 336 km s^{-1}, has a ratio between the polar radius and the equatorial radius of ~ 0.7 and $T_{pole} - T_{eq} = 3500$K (Che et al. 2011).

1.1.1 Modelling Rotating Stars

In the interior of a rotating star centrifugal forces reduce the effective gravity depending on the latitude and also introduce deviations from sphericity. If such stars are to be modeled, the four equations of stellar structure need to be modified, and introducing all the effects imposed by rotation into the calculation of realistic models that can be compared to observations have been quite a challenge for several decades. Several approximations has been made trying to simplify the problem; the most famous approximation still used today is known as von Zeipel's law (1924). He showed that uniformly rotating models have the state properties constant on equipotential surfaces, and under the condition of radiative equilibrium, the star has a local surface flux that is proportional to the local gravity, $F \propto g$. Using the Stefan-Boltzmann law, where $F = \sigma T_{eff}^4$, von Zeipel's law implies that $T_{eff} \propto g^{0.25}$. Actual observation and application of this relation however, indicate that slightly different exponents of the gravity appear to provide a better match to the deduced properties, so a general parametrization of the relationship between the effective temperature and the gravity is often used: $T_{eff} \propto g^{\beta}$ (Lucy 1967; Kippenhahn 1977; Maeder 1999). This relation is a common tool used to simplify the calculation of the surface properties of a rotating star where the potential, assuming the Roche potential for the gravitational potential, can be expressed as

$$\Phi = \frac{GM}{R(\theta)} + \frac{1}{2}\omega^2 R(\theta)^2 \sin^2\theta = \text{constant}. \tag{1.1}$$

For this potential, the two components of the effective gravity in polar coordinates can

be easily found to be,

$$g_r(\theta) = -\frac{d\Phi}{dr} = -\frac{GM}{R(\theta)^2} + \omega^2 R(\theta)\sin^2\theta \qquad (1.2)$$

and

$$g_\theta(\theta) = -\frac{1}{r}\frac{d\Phi}{d\theta} = R(\theta)\omega^2\sin\theta\cos\theta. \qquad (1.3)$$

Here G is the gravitational constant, M is the mass, ω is the angular velocity and θ is the colatitude. The magnitude of the effective gravity at any latitude θ can be calculated from $g_{eff} = \sqrt{g_r^2 + g_\theta^2}$ (Aufdenberg et al. 2006) and finally from von Zeipel's law one can find the effective temperature for any given latitude.

There are, however, several shortcomings with the method described by von Zeipel. The assumption of a stellar surface that can be described with a Roche potential only holds for stars whose density distribution in the deep interior is not perturbed from a spherical distribution. Such stars include all uniform rotating cases except those rotating exceedingly close to critical rotation (Lovekin et al. 2006). Moderately and rapidly rotating stars with rotation rates increasing with decreasing distance from the rotation axis can not be described by a Roche potential and the actual gravitational potential must be calculated. Equation 1.1 does not hold for non-conservative rotation laws because in that case there is no such thing as a potential by definition. One other concern with von Zeipel's law is the decoupling of the effective temperature and the surface temperature. The von Zeipel's theorem assumes that the temperature is constant along an equipotential surface, includ-

ing the stellar surface, while in an actual rotating star the effective temperature is varying from pole to equator.

Von Zeipel's result in which the state variables are constant on equipotential surfaces led to the development of two computational approaches for calculating rotating stellar models in the late 1960's. One of these approaches, the self-consistent field method (Ostriker & Mark 1968), solved for the gravitational potential for a given density distribution and then solved for a new density distribution on equipotential surfaces from hydrostatic equilibrium. The new densities led to a new approximation of the gravitational potential, and the entire process was iterated until all changes were sufficiently small. Jackson (1970) modified this method to include thermal equilibrium as well and has computed a number of rapidly rotating stellar models (Jackson et al. 2004,2005; MacGregor et al. 2007). Bodenheimer (1971) also used the method to compute a number of rapidly rotating main-sequence models for several angular momentum distributions. Clement (1974; 1978; 1979) modified the original double series expansion for the gravitational potential with a two-dimensional (2D) finite-difference approach.

The second approach, developed by Monaghan & Roxburgh (1965) and extended and utilized by others (e.g., Roxburgh et al. 1965; Faulkner et al. 1968; Kippenhahn & Thomas 1970; Sackmann & Anand 1970), allowed certain rotating models to be calculated in a one-dimensional (1D) framework. This approach was extended by Endal & Sofia (1976; 1978) to include the redistribution of angular momentum in this 1D framework for a number of hydrodynamic and thermal instabilities, and such prescriptions are now commonly included in stellar evolution codes (e.g., Demarque et al. 2007; Eggenberger et al. 2007).

An alternative to these methods is to solve for all of the appropriate equations and their boundary conditions simultaneously on a 2D grid (e.g. Clement 1978,1979; Deupree 1990,1995; Espinosa Lara 2010). The reason for using this framework was to include the appropriate velocity terms in the conservation equations to compute features such as meridional circulation. However, it can also be used to calculate the stellar structure of isolated models as well as members of evolution sequences.

After the stellar structure is obtained, the surface values of these models can be used as input to construct an appropriate emergent flux that includes the effects of the surface variation of the relevant properties of the star. This can be done by performing an integration over the visible surface of the star of the intensities emerging from many atmosphere models that are defined by the local surface parameters of the star. Collins (1963) was one of the first ones to attempt such atmospheric modeling by using von Zeipel's law, uniform rotation and grey atmospheres where the radiative transfer equation was greatly simplified. One of the most significant conclusions from his work was how much the observed luminosity of a rotating star depended on the angle at which it was observed. Later refinements using various atmospheric models to describe a single rotating star confirmed those early results (e.g., Collins et al. 1991; Collins & Truax 1995). More improvements would come from the level of realism included in the atmosphere modeling. Maeder & Peytremann (1970) computed LTE atmospheres where the hydrogen line opacities for the Balmer and Lyman series were included. Slettebak et al. (1980) and Frémat et al. (2005) added more realism by using a series of non-LTE atmospheres in their models.

The next step after a satisfactory atmospheric model is achieved is to determine observ-

able properties from this synthetic set up. In general, a model atmosphere will produce the intensity emerging from the atmosphere as a function of the direction with respect to the local surface normal. If one takes the component of each set of rays in the direction of the observer, it is possible to determine the flux at each wavelength that will be observed at some distance from the star. The general expression for this integration in spherical coordinates would be:

$$F_\lambda(i) = \int_\theta \int_\phi I_{\lambda'}(\xi(\theta,\phi,i))W(\lambda,\lambda')\frac{\mathrm{d}A_{\mathrm{proj}}\cos\xi(\theta,\phi,i)}{d^2}, \tag{1.4}$$

where ξ is the angle between the local normal to the surface and the direction to the observer, $W(\lambda,\lambda')$ denotes the wavelength change produced by the Doppler shift, and the element of projected area, $\mathrm{d}A_{\mathrm{proj}}$, is given by

$$\mathrm{d}A_{proj} = R^2(\theta)\sin\theta\cos\xi\sqrt{1+\left(\frac{\mathrm{d}R}{\mathrm{d}\theta}\right)^2\frac{1}{R^2}}\mathrm{d}\theta\mathrm{d}\phi. \tag{1.5}$$

This flux will provide the spectral energy distribution (SED), and from the SED quantities like the observed luminosity and the colors in any band can be calculated. For a rotating star the same principle applies, but there would be a dependency between all the observable quantities and the angle with respect to the rotation axis at which the observation is set to be made. This whole procedure can become difficult and highly computer intensive, so as expected, approximations have been made to ease the reproduction of such observables. The most important is known as the limb darkening law (Carroll 1928, 1933; Shajn & Struve 1929), in which the star is treated as a circular disk in which the edges of

the disk or "limbs" will contribute less intensity to the total flux, hence the "darkening" on those zones. Slettebak (1949) applied this idea to rotating stellar models where the deformation at the equator will reduce the effective gravity, and recalling von Zeipel's theorem, this will reduce the flux coming out of this area, producing an equivalent effect to the limb darkening similarly called gravitational darkening. In the end, one would expect that the method in which the actual intensities coming out of each zone in the atmosphere of the star are integrated would produce more realistic results. Both the limb darkening and the gravitational darkening are automatically incorporated in this calculation without any restrictive assumptions.

The final test of all the effort put into the modeling of these stars comes from comparison with real known rotating stars. Stellar rotation studies have struggled here because the only measurable trace of rotation in a stellar spectrum was $v \sin i$. That left a large set of unknowns only very weakly constrained within the models, and great levels of degeneracy on parameters such as the inclination, R_{eq} and R_{pole}, T_{eff} at the equator and the pole, the internal angular momentum distribution, among others. Fortunately, in the last decade, great advances in instrumentation have allowed asteroseismology and optical interferometry to provide the determination or constraint of many of these free parameters. Asteroseismology provides a good test for the internal structure of the star, while interferometry is allowing direct resolved observations of deformed rotating stars, providing their inclination and their oblateness. Good candidates have surfaced such as the rapidly rotating star Achenar (Domiciano de Souza et al. 2003) but this early attempt was clouded by the possibility that a circumstellar envelope was contributing to the oblateness measured

by the interferometry as well as the stellar surface (Vinicius et al. 2006; Kanaan et al. 2008; Carciofi et al. 2008; Kervella et al. 2009). It was possible to successfully reproduce the observed shape (Jackson et al. 2004) but only with a markedly differentially rotating model. Several various other rapidly rotating stars have now been successfully resolved by interferometry. One of these stars, α Oph, will be the focus of this work as it has proven to be great test case to model for reasons that will be discussed in the next section.

1.2 α **Oph**

The search for a good candidate to test current stellar interior structure models that include rotation led us to the brightest star in the constellation of Ophiuchius. α Oph itself is a binary system with an extremely eccentric orbit of $e = 0.92 \pm 0.03$ (Hinkley et al. 2011) and a period of 8.62 years. An interesting fact is that the companion, a K2 V star, makes a very close approach (~ 0.50AU) at periastron. Also of interest is that the orbital plane ($i = 125° \pm 8°$) is not aligned with the rotational equator of the main star. In this work the binary nature of α Oph is not relevant, but the dynamical evolution of the star (particularly its angular momentum history) may have influenced the properties of the principal member in the binary system. It is also important to note that the dwarf companion contributes only an estimated 1.2% of the observed flux in the red (van de Kamp 1967). For notation purposes we will refer to the primary, the one we're interested in, of the system as simply α Oph. Classified as an A5IV δ Scuti star, α Oph (=HR 6556, HD 159561) is the seventh brightest A-type star in the sky and has an observed $V_{eq} \sin(i)$ of about 240 km s^{-1} (Royer

et al. 2002). This is sufficiently large for the rotation to have appreciable effects on at least the surface conditions.

It was observed interferometrically with the CHARA array by Zhao et al. (2009) and asteroseismologically with the MOST satellite (Monnier et al. (2010)). The interferometry revealed that α Oph is seen nearly equator on, with a ratio of the polar radius to the equatorial radius of about 0.836. A summary of the key observed properties is given in Table 1.1. An important note to the observed properties is that the deduced mass was derived from the orbital solution of the binary system, which provides a more fundamental and accurate measurement than a mass estimated by its location in the HR diagram. The observed luminosity and effective temperature (i.e., those quantities deduced assuming that the observed flux is produced by a spherical star) range from 7880 to 8050K for the effective temperature and from 25.1 to 25.6 $L_\odot$ for the luminosity (Blackwell & Lynas-Gray (1998); Malagnini & Morossi (1990); Monnier et al. (2010)). These values should be quite accurate given that the star has a well-determined parallax (see discussion in Gatewood (2005)), and there is insignificant reddening. These results also place the star relatively close to the blue edge of the instability strip (e.g., Breger 2000; Xu et al. 2002). However, the perceived effective temperature and luminosity depend on the inclination between the observer and the rotation axis, and the actual luminosity and effective temperature for a rapidly rotating model seen equator on will both be higher than perceived, possibly placing α Oph even closer to the blue edge. One desirable consequence of this is that atmospheric convection is likely not significant and can be ignored. The combination of the deduced luminosity, effective temperatures at the pole and the equator, the observed oblateness, surface equatorial velocity

and inclination, limit even more the possible models for this star.

To determine the precise relationship between those observed properties and the actual ones requires the calculation of the spectral energy distributions which can be compared with observations of α Oph. Instead of applying the often used limb and gravity darkening assumptions to calculate the SED (e.g., Claret 2003; Reiners 2003; Townsend et al. 2004; Monnier et al. 2010), a more rigorous approach would be to integrate the weighted intensity coming out of the star in the direction of the observer over all the visible surface using the latitudinal variation of the radius, the local effective gravity and the local effective temperature to obtain the observed flux (e.g., Slettebak et al. 1980; Linnell & Hubeny 1994; Frémat et al. 2005; Gillich et al. 2008). Rotating models whose properties match the observed spectral energy distribution, the surface equatorial velocity, and the oblateness would appreciably confine at least the surface stellar rotation properties. The other key component available in this case is the ability to check how well the internal structure models match the pulsation modes observed. Analysis of the MOST data for α Oph revealed 57 oscillation frequencies which clearly must include both p and g modes. The combination of the comparatively large number of oscillation modes and the relatively detailed knowledge about the stellar properties make α Oph a good candidate to explore specific problems that might be encountered when trying to match the entire collection of data. It is important to note that none of the oscillation frequencies has a half amplitude larger than 0.7 mmag, so that we do not have to be concerned about the variation of the atmospheric properties with pulsation phase in simulations of the SED or the spectral lines.

Deupree (2011) performed both 2D stellar evolution simulations and linear, adiabatic,

Table 1.1
Observed properties of αOph

Property	Observed Value
Spectral Type	A5 III
V	2.08[1,2,3]
$(B - V)$	0.15[1,2,3]
$(U - B)$	0.10[1,2,3]
R_{pole}/R_{eq}	0.836[4]
[Fe/H]	-0.14[11]
T_{eff}	7880K-8050K[12]
Distance	14.68[5]
V_{eq} (km s^{-1})	210-240[6,7,8,9]
Inclination (deg)	87.5[9]
Mass	2.4[10]

References: (1) Johnson & Harris 1954; (2) Johnson & Knuckles 1957; (3) Johnson et al. 1966; (4) Monnier et al. 2010; (5) Gatewood 2005; (6) Bernacca & Perinotto 1970; (7) Uesuga & Fukuda 1970; (8) Abt & Morrell 1995; (9) Royer et al. 2002; (10) Hinkley et al. 2011; (11)Erspamer & North (2003); (12) Zhao et al. 2009.

nonradial oscillation calculations of α Oph with models that reproduced the mass, oblateness and the surface value of equatorial velocity, within error, finding that comparison between observed and computed frequencies for a moderately rapidly rotating star indicated that several issues must be resolved before one can comfortably conclude that any computed model of a sufficiently rapidly rotating star is an adequate fit. Using those models as ground work we attempted a match of the SED (Deupree et al. 2012) by integrating the weighted intensity coming out of the surface of the star in the direction to an observer at earth. We succeeded in finding a model with solid body rotation that reproduced the observed SED of α Oph closely. It was also better than the SED of a spherical model counterpart with the deduced effective temperature of the star. The model was also used to test its oscillation properties; when compared to the pulsation modes observed, the five highest and seven of the nine highest amplitude modes show agreement between computed

axisymmetric, equatorially symmetric mode frequencies within the observational error. Including nonaxisymmetric modes up through $|m| = 2$, and allowing for the possibility that the eight lowest amplitude modes could be produced by modes that are not equatorially symmetric, it matched 24 out of the 35 MOST modes to within the observational error.

Based on a comparison of these frequency results with those of Deupree (2011), it is clear that being able to match the observed SED in both the visual and ultraviolet plays a crucial role in constraining the model but still issues remain. The most important of these is perhaps the internal angular momentum distribution. It is clear that the model reproduced the surface values closely with uniform rotation, leading to the expectation that the star may not be too far from uniform rotation, at least near the surface. This assumes that the surface is an equipotential, something that, while not unreasonable, remains an assumption. One would expect for a star as evolved as α Oph that a more reasonable angular momentum distribution would not correspond to a conservative rotation law because at least part of the core would be rotating more quickly than the surface, even at the pole, in which case no equipotential can be defined. The next natural step in the investigation is to test different models that have non uniform internal angular momentum distributions, which is the intention of the present work. The next chapter present the steps in the calculation procedure, same as the one used in Deupree et al. (2012), to obtain the SEDs of those models.

Chapter 2

Methods

2.1 The synthetic SED of a rotating star

In order to compute observable quantities other than the total luminosity of a rotating star, it is not enough to just model its possible interior structure. All the radiation we observe or measure from any star comes from its atmosphere, and although the internal structure will set up the conditions of such an atmosphere, a good model is necessary to succeed in creating a realistic spectrum. The SED is one of those observables that require a good atmosphere calculation, and when stellar rotation is included, this atmosphere model must take into account all the effects that a rotating star has with its latitudinally varying surface parameters. Various SEDs were calculated for comparison to observations of α Oph. A detailed procedure of how they were obtained is presented below.

The methodology used is based on the work of Lovekin et al. (2006) and Gillich et al. (2008) which consists of 3 steps to obtain the spectra: The first is the calculation with RO-

TORC of a fully 2D stellar evolution model that includes rotation (Deupree 1990; 1995; 1998). This model will provide the surface values of effective temperature and effective gravity at each point on the surface of the deformed star. The second step is the calculation of plane parallel atmospheres with the PHOENIX model atmospheric code. The variation of temperature and gravity with the colatitude of the star requires the computation of a whole grid of different atmospheric models that will cover all the possible values of temperature and gravity given by the ROTORC model. The assumption is that the emergent intensity at any point on the surface can be approximated as that for a plane parallel model atmosphere with the local effective temperature and surface gravity. Using various plane parallel atmospheres is a good approximation in this case because any significant horizontal variation is apparent only over many photon mean free paths, and the radial extent of the atmosphere is very small in comparison to the stellar radius. The actual atmosphere of the rotating stellar model will be generated from the atmosphere grid by interpolating the intensity rays emerging from the surface of each plane-parallel PHOENIX model as a function of angle from the normal to the surface. In the last step, CLIC, a code developed by Lovekin et al. (2006), will be used to perform the numerical integration of these intensities over the observed surface of the star to obtain the SED one would observe at a user-specified distance and inclination with respect to the axis of rotation of the star. Each component of the modeling process is detailed in the next sections.

2.1.1 ROTORC

ROTORC is a fully implicit 2D hydrodynamics and hydrostatics stellar evolution code developed by Deupree (1990,1995) to determine the structure of rotating stellar models. In this context, ROTORC provides the effective temperature, effective gravity, radius, and rotational velocity at the surface as a function of latitude. There are no specific requirements about the angular momentum distribution, although the surface location at each latitude is found as if the surface were an equipotential. Time-dependent equations of momentum, thermal balance, along with Poisson's equation, the equation of state, and relations for the nuclear energy generation and the radiative opacity are solved simultaneously for the density, pressure, temperature, velocity in three dimensions and gravitational potential at each location in a 2D grid. It should be noted that ROTORC does not assume a Roche potential. ROTORC was used in a mode where the rotational velocities can be imposed through a rotation law and the velocities in the radial and latitudinal direction reflect only the stellar evolution. The method of solution is a two-dimensionalization of the Henyey technique outlined by Deupree (1990). In this method, for each zone in the grid, a first guess for all of the unknown variables is made and the difference equations are expressed as first-order expansions in corrections to all the unknown variables. Then, by the equivalent of a matrix inversion, a simultaneous solution for all the first order corrections is found, giving a second approximation to the actual solution. The process is iterated until the corrections are considered to be small enough and the result can be used as an initial guess for the next time step in the evolutionary sequence. Since all equations, boundary conditions and
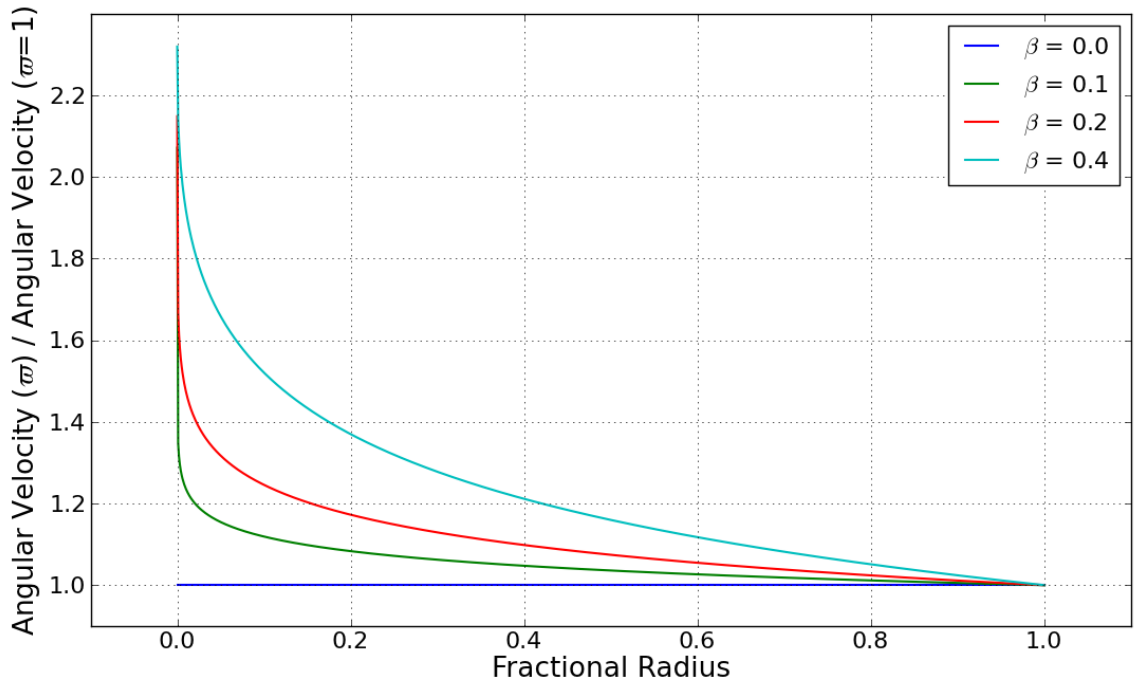
Figure 2.1: Illustration of various differential rotation laws for different values of β. The value of a was chosen to be 2 and ω_0 is $1 + a^\beta$ for this specific plot.

global conditions are simultaneously included, convergence is expected.

Another important feature in ROTORC is the inclusion, if desired, of differential rotation in the simulation. One specific differential rotation law of interest for this work follows the relation:

$$\omega(\varpi) = \frac{\omega_0}{1 + (a\varpi)^\beta} \tag{2.1}$$

Here ω is the angular velocity and ϖ is the distance to the rotation axis. The quantities of ω_0, a, and β, are constants, and they define how much differential rotation is included. We note that this rotation law is conservative because it depends only on ϖ. It's easy to see

from equation 2.1 that solid body rotation is recovered when $\beta = 0$. Figure 2.1 shows the different rotation laws that will be considered in this work.

2.1.2 PHOENIX

PHOENIX (Hauschildt & Baron 1999) is a non-LTE stellar atmosphere and spectrum synthesis code that generates (for our purposes) 1D plane-parallel models by solving the equations of hydrostatic equilibrium, thermal equilibrium, equations of state and the equation of radiative transfer:

$$\frac{dI_\lambda}{d\tau_\lambda} = I_\lambda - \frac{j_\lambda}{\kappa_\lambda}, \tag{2.2}$$

where τ_λ is the optical depth at the specific wavelength λ. The ratio of the emission and absorption coefficients, j_λ and κ_λ, is known as the source function $S(\lambda)$.

PHOENIX is commonly used in a two step process in which initially a stellar structure model of the atmosphere is converged, and finally, the code finds the formal solution of the radiative transfer equation to synthesize a spectrum.

The code is capable of keeping track of the population of thousands of atomic energy levels, and the calculation can be performed under two different regimes: local thermodynamic equilibrium (LTE) or non-LTE (NLTE). LTE assumes equilibrium between matter and the local radiation field, with the electron population of atomic energy levels described by Boltzmann statistics, the ionization equilibrium by the Saha equation, and the source function of the radiation field, S_λ, by the Planck function $B_\lambda(T)$. However,

Table 2.1
Species treated in NLTE

Element	I	II	III	IV
H	50/1225	-	-	-
He	19/37	10/45	-	-
Li	57/333	55/124	-	-
C	228/1387	85/336	79/365	-
N	252/2313	152/1110	87/266	-
O	36/66	171/1304	137/765	-
Ne	26/37	-	-	-
Na	53/142	35/171	-	-
Mg	273/835	72/340	91/656	-
Al	111/250	188/1674	58/297	31/142
S	146/439	84/444	41/170	28/50
K	73/210	22/66	38/178	-
Ca	194/1029	87/455	150/1661	-
Fe	494/6903	620/13675	566/9721	243/2592

the mean intensity of the radiation field, J_λ, will in general depart from the value of B_λ expected in strict thermodynamic equilibrium (TE). This can be a very helpful simplification but it is an unrealistic approximation in some cases. The case of NLTE makes the more general assumption of the existence of a steady state statistical equilibrium between matter and radiation, which necessitates the explicit solution of atomic level populations (or occupation numbers) from the coupled rate equations. Table 2.1 shows the species selected to be treated in NLTE in this work. See Short et al. (1999) for a complete list.

For those species treated in NLTE, only energy levels connected by transitions for which $log(gf)$ is greater than −3 (designated primary transitions) in the PHOENIX line list are included in the NLTE statistical equilibrium equations. All other transitions (secondary transitions) for that species are calculated with occupation numbers set equal to the Boltzmann distribution value with the excitation temperature equal to the local kinetic temper-

ature, multiplied by the NLTE departure coefficient for the ground state in the next higher
ionization stage.

The energy level and bound–bound transition atomic data have been taken from Ku-
rucz (1994) and Kurucz & Bell (1995). The resonance-averaged Opacity Project (Seaton
et al. (1994)) data of Bautista et al. (1998) have been used for the ground-state photoion-
ization cross sections of Li (I–II), C (I–IV), N (I–VI), O (I–VI), Ne (I), Na (I–VI), Al (I–VI),
Si (I–VI), S (I–VI), Ca (I–VII), and Fe (I–VI). For the ground states of all stages of Mg, P,
Ti and for the excited states of all species, the cross-sectional data previously incorporated
into PHOENIX from either Reilman & Manson (1979) or from the compilation of Mathisen
(1984) was used. The coupling among all bound levels by electronic collisions is calculated
using cross sections calculated from the formulae compiled by Allen (1973). The cross sec-
tions of ionizing collisions with electrons are calculated from the formula of Drawin (1961).

2.1.3 CLIC

The intensity integrator code, developed by Lovekin et al. (2006) and later modified and
used by Gillich et al. (2008), is a tool for calculating the SED of a rotating star model. It
computes as a function of wavelength the flux an observer would measure outside Earth's
atmosphere for a star at a specified distance. As input, CLIC needs the surface properties
of the stellar model of interest: radius, effective temperature (T_{eff}), the logarithm of the
effective gravity ($log(g)$) and the rotational velocity as function of colatitude. These are
are provided by ROTORC. To model the atmosphere of the star the whole non spherical
surface is divided into a mesh of 200 zones in θ and 400 zones in ϕ in which the intensities

emerging from each piece of stellar surface of the star in the direction of the observer, $I_\lambda(\xi(\theta,\phi,i))$, are obtained from interpolation through the grid of the appropriate plane-parallel model atmospheres generated by PHOENIX. Including the entire surface allows the flux the observer would see to be determined at any arbitrary inclination.

The observed flux is then calculated as a weighted integral of those intensities coming out of each zone over the visible surface of the star (equation 1.4). The visible surface will depend on the inclination with respect to the local vertical direction of the star at which the surface is being observed. The integral is calculated for each wavelength with a separation $\Delta\lambda = 0.02\text{Å}$, which provided a good sampling of the line profiles, especially in the UV. This wavelength separation is also better than the resolution of the data to be discussed later. The geometry of the problem is fully described by Lovekin et al. (2006).

The program is set up to output ten different fluxes corresponding to ten different observed inclinations with respect to the star pole, starting with $i = 0°$ (pole on view) to $i = 90°$ (equator on view) in 10 uniform steps. An example of the different SEDs obtained for a model with $V_{eq} = 233\,\text{km/s}$ and mass of $2.2M_\odot$ as a function of inclination with respect to the star's vertical is shown in Figure 2.2. The code can be easily modified to compute the observed flux for any desired inclination. In our case, we set up CLIC to compute the flux at the deduced inclination of α Oph, 87.5°.

The SED is intended to cover a large part of the spectrum, usually with flux averages computed after that, so broadening effects on individual lines are not considered. This allows the decoupling of individual wavelengths, making the calculation ideal for parallel processing. When considering small regions of the spectrum, CLIC has a subroutine that
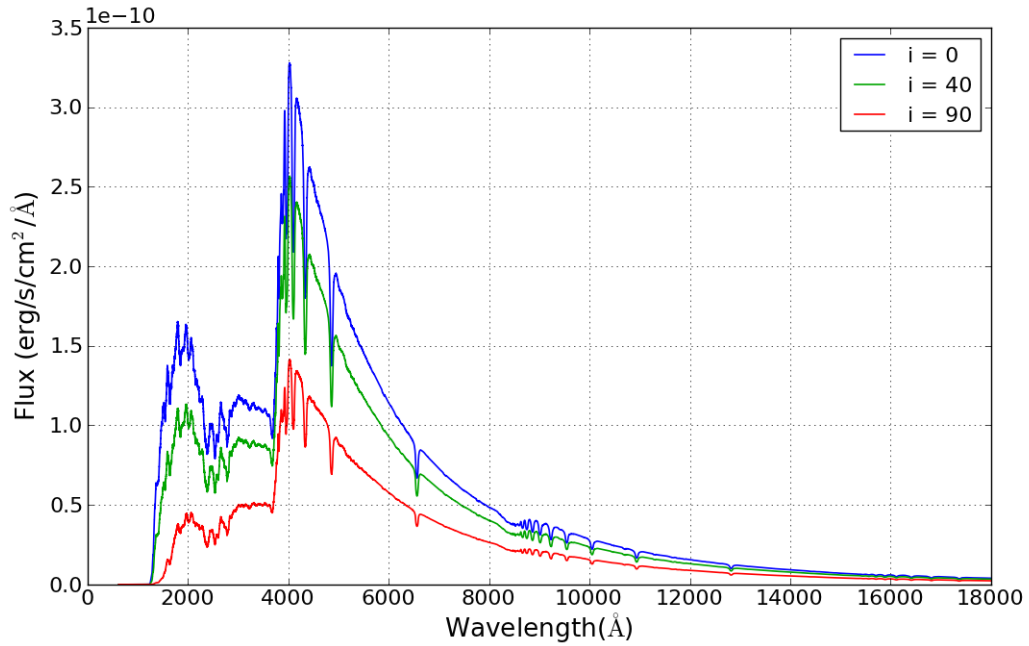
Figure 2.2: CLIC calculated SED for 3 different inclinations of a specific rotating model filtered with a boxcar filter of $50\mathring{A}$.

can include Doppler broadening over $100\mathring{A}$ wide sections in the spectrum intended for the analysis of individual line profiles. The process of calculation is the same one used for SED computation, except that a second flux array is used to perform the wavelength shift.

2.2 This work

αOph presents an ideal case to study the stellar interior of a rapidly rotating δ Scuti star given the number of constraints (e.g. both interferometric and asteroseismic) that possible models need to match. A previous attempt to match the p-modes has already been done by Deupree (2011) and as a conclusion from this work he proposed that a rotational model that could match the SED and the vibrational modes of the star may be a better indicator

of the actual internal structure of αOph. As a follow up, we showed that a stellar model that includes rotation fits the observed properties of the SED better than a simple spherical non-rotating one (Deupree et al. 2012). This last work considered only solid body rotation, and as discussed in Section 1.2, for an evolved star like αOph, uniform rotation is probably unrealistic. We can make a crude estimate of the amount of differential rotation a star like α Oph in the latter phase of core hydrogen burning would have in the following manner. We assume that the star was uniformly rotating on the Zero Age Main Sequence and that it locally conserves angular momentum (except maybe in the convective core) during its evolution. We then compare the angular momentum distribution along the equator between the centre and surface of the model with the distributions imposed by equation 2.1 for various values of beta. This distribution resembles that from the equation with $\beta = 0.4$ except near the centre, where the angular momentum redistribution by convection makes any result questionable in any event. This can only be an approximation because we impose a conservative rotation law in a situation for which it is probably false. Nevertheless, the $\beta = 0.4$ rotation case may be a reasonable upper limit to the amount of differential rotation for this form of the rotation law.

The generation of the synthetic SEDs of αOph follow the recipe described before and used by Lovekin et al. (2006) and Gillich et al. (2008), using the ROTORC models with non-uniform internal angular momentum distributions given in equation 2.1. Various possible 2D internal structure models of α Oph which have the observed oblateness and other surface parameters were produced to compare with the observed SED when placed at the proper distance. After comparing the broadband SED we checked the profile of 12 differ-

ent individual lines and features including the Doppler broadening product of the stellar

rotation. With both the full SED and the lines we test if it is possible to deduce the existence

of differential rotation in the interior of the αOph.

Chapter 3

Matching the SED of α Oph

We calculated a grid of PHOENIX NLTE model atmospheres covering values of T_{eff} between 7500K and 9250K in steps of 250K, and for each temperature a range of values of $log(g)$ between 3.333 and 4.0 with a step of 0.333. All models were calculated with solar composition. As previously mentioned, we need to cover all the surface properties of the stellar models provided by ROTORC. A typical microturbulence velocity value for a late A star (Gray et al. 2001) of 2km s^{-1} was used in each plane parallel model atmosphere. It is important to note that this parameter will not have a great impact on the line broadening process compared with the broadening effects caused by the rapid rotation of α Oph. The emergent intensities of these plane parallel atmospheres were calculated between 600Å and 20 000Å at a variable step size in wavelength in order to try to keep a resolution $\lambda/\Delta\lambda$ higher than 200 000, which is sufficient to resolve most features in the spectrum. The wavelength range selection was done when the integration of the flux between these wavelengths and the theoretical luminosity given by the Stefan-Boltzmann

law for the T_{eff} for the atmospheric model agreed to within 1%. An important aspect to note about PHOENIX is that it must automatically "add" wavelength points in between the specified values of $\Delta\lambda$ if it detects that there is a NLTE spectral line that will be missed in the current wavelength step. The calculation of each NLTE atmosphere is relatively computer intensive, sometimes needing more than 48 hours of 4 CPUs working in parallel to converge a a single model.

After finishing the grid, and in conjunction with the ROTORC model of interest, we used CLIC to obtain the SEDs at ten different inclinations with respect to the line of sight. The SED is set up to have a $\Delta\lambda = 0.02$Å and is calculated from 1000Å to 20 000Å which gives more than enough resolution to critically sample most of the absorption features in the spectra of α Oph, and also to compute different deduced properties such as the intrinsic colors, the observed luminosity and the deduced effective temperature. This starting wavelength was used for the CLIC synthesis in comparison with the atmospheric model files after observing that the flux contribution between 600Å − 1000Å was minimal. The observed luminosity in this synthetic case will be simply the integral of the SED in the wavelength range considered, adding the contribution of the Rayleigh-Jeans tail with the analytical approximation after 20 000$\mathring{A}$ to account for any missing flux beyond our upper wavelength limit. For the most part we considered a single inclination of the CLIC output file that corresponds to $i = 87.5°$, set up to match the observed inclination of α Oph. Finally, SED fluxes were scaled to reflect the 14.6pc distance of α Oph (Gatewood 2005). Interstellar extinction can be determined from the color excess of $E(B − V) = 0.01$mag (Crawford (2001)). This by itself is a relatively small value, so small that it does not have

many significant digits and may be hard to accurately include. For our models interstellar extinction was assumed to be zero.

We also want to compare our rotating model SEDs with that for a spherical model that best fit the SED on the visible part of the spectrum. The effective temperature for the spherical model was $7875K$. The SED for the spherical model was calculated in the same way as the SEDs for the rotating models.

We examined various observed data sets of $α$ Oph in regions of the visible and ultraviolet part of the spectra to compare with the computed SEDs. For the visible region we used the data set L1985BURN, file 01398 of the HyperLeda catalog (Paturel et al. (2003)) and based on the spectrometry of Burnashev (1985). SED measurements in the UV were found from the IUE and OAO2 space observatories for wavelengths between $1200Å$ and $3000Å$. The IUE data considered came from sets SWP17411 $(1150Å - 1900Å)$ and LWR05927 $(1900Å - 3200Å)$ downloaded from the MAST online archive administered by STScI. It is not the only set available but it is one of the most complete in the whole UV wavelength range. The OAO2 data were obtained from Code & Meade (1979). The resolution of the IUE data was 100 times higher than the OAO2 counterpart, but the standard deviation associated with each flux measurement in the spectrum was much lower for the OAO2 data. To obtain comparable datasets with similar spectral resolution, the finely sampled IUE spectrum was convolved with a boxcar filter of width 50A. A Monte Carlo technique was used to estimate the uncertainty in these filtered fluxes. In each iteration, the IUE flux measurement at each sampled wavelength was randomly (and independently) varied by a value drawn from the gaussian distribution defined by the quoted IUE $1σ$ flux

uncertainty. This perturbed data set was then convolved with the 50A boxcar filter. After 1000 Monte Carlo iterations, the mean and standard deviation of the resulting fluxes at each sampled wavelength were computed. Figure 3.1 shows a comparison between the OAO2 and the IUE observations. Although the two agree at some wavelengths within the uncertainty, there are many wavelengths at which they do not. There will be models that we can match to either one of the observed data sets. For this work we chose to compare our synthetic SEDs with the IUE flux distribution given it's high resolution which also allowed comparison of fine details such as individual line profiles. Putting together the IUE and visual data also carries some complications because they do not overlap in the UV and there is no reference of which one provides better flux measurements in this region.

For this work, one suite composed of 4 different ROTORC models with different angular momentum distributions was selected as the best fit to the observed SED. All of them were calculated to have the same observed shape and other basic parameters of α Oph (see Table 1.1). The next subsection will give a description of how these models were calculated.

3.1 Rotating Models

During an attempt to match the p-mode oscillation modes, Deupree (2011) found a model identified as "V240" which had the observed oblateness. However, a comparison of the observed SED with the computed SED at the α Oph inclination showed that the model effective temperature was too high. New models were obtained by performing a few evolutionary time steps (thus moving to cooler effective temperatures), which change the com-
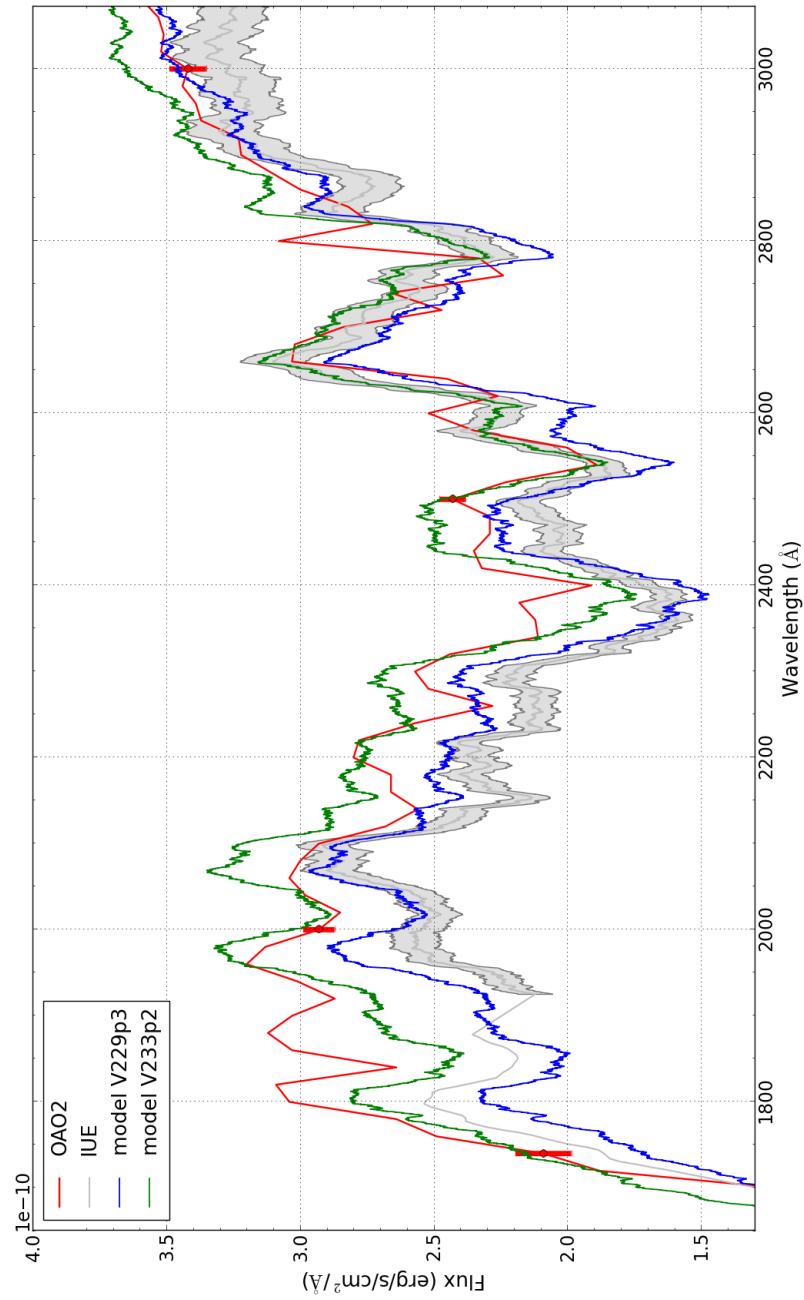
Figure 3.1: Ultraviolet data from the IUE and OAO2 missions compared

position in the convective core and the surrounding area as the convective core shrinks. During this "evolution" the shape is the only surface characteristic that is held constant. The surface rotation velocities are no longer those required for an equipotential surface to match the current (desired) surface shape, so the uniform rotation rate was scaled and the model at the end of this evolution sequence re-converged, a process continued until a uniform rotation rate was found which produced an equipotential surface that matched the desired surface shape. Only a few evolutionary times steps were done at a time so that the change in the surface equatorial velocity was only a few km s^{-1}. The entire process is repeated until there are a sufficiently large number of models with composition profiles that look like those at various stages of an evolutionary sequence. Thus, these models form a sequence of constant surface shape but decreasing effective temperature. It should be noted, however, that these are not strictly speaking evolutionary sequences because we have artificially constrained the rotation during the evolution in a way that does not conserve angular momentum. From the point of view of creating a 2D stellar model that can be compared with data, not having obtained the model by a direct evolutionary sequence calculation is irrelevant. We found a possible matching model (Deupree et al. 2012) denoted V236_Xc25 that came from testing different parameters in the ROTORC model calculation. This model not only matched the SED well (better than a spherical model would) but was also able to match several high amplitude observed p-mode frequencies. Still, two issues remained with V236_Xc25: one was the fact that the model didn't come from an evolutionary path (it came from seemingly arbitrary changes of the stellar interior to get the right shape and surface equatorial velocity) and the other the fact that the model represented

a uniformly rotating star. All of ROTORC calculations mentioned above were performed with the hydrogen mass fraction and the metals mass fraction of 0.7 and 0.02, respectively. This abundance was used for all ROTORC calculations in this thesis, as well.

Having V236_Xc25 surface parameters as reference and still assuming uniform rotation for simplicity, a new set of ROTORC calculations were performed by Dr. Deupree to obtain a model that would be part of a evolution sequence and would also have the same shape, surface temperatures and surface equatorial velocity. From this new set, the model V233p2 seemed like a perfect candidate matching most of V236_Xc25 surface values suggesting that the calculated SED should have been very close between the two models, but instead we found a some unexpected differences between them.

After careful examination we found that the difference came from non-uniform wavelength vectors in the different PHOENIX model atmosphere files. This conflicts with the CLIC execution, which expects an atmospheric grid with uniform values of wavelength (same number of points and values) between all the intensity files. When V236_Xc25 was calculated not all the PHOENIX intensity files had been cleansed of the added wavelengths and later when the SED calculation of the V233p2 model was required, all the atmospheric PHOENIX files had been interpolated in wavelength to have a $\Delta\lambda = 0.02$. A recalculation of the SED produced by the V236_Xc25 model using the interpolated PHOENIX files showed that it was very similar to the one of V233p2, as we initially expected.

Fixing this issue left the V236_Xc25 and V233p2 SEDs as a couple of models that didn't fit the IUE observations quite as well as before although still generally within the range between the OAO2 and the IUE SED curves (see figure 3.1), so a new search for a uniformly

rotating model was done. The work was not excessively complex given the fact that we already knew which set of parameters we wanted to match and many models close to them already existed.

After several iterations of SED comparisons, we found a uniformly rotating model, ID V229p3, that best fit the observations. As evident from figure 3.1, which of the two models, V233p2 or V229p3, fits the observations better depends on whether one gives more or less weight to the OAO2 data in comparison to the IUE data. Clearly, more accurate ultraviolet data would be invaluable in constraining the properties of the rotating models. From V229p3 Dr. Deupree developed three other stellar models with slightly different internal momentum distributions that still preserved the ratio of the polar to equatorial surface radius of α Oph. With this set we want to test if it is possible to determine whether the star is differentially rotating just from the SED. Equation2.1 describes the differential rotation law used to impose the internal rotation profile. Knowing that differential rotation changes the shape of the star (thus changing the surface values), we looked for a range of values of β that would produce a ROTORC model whose surface values still matched the observed properties of α Oph within observational error. With a fixed to 2, the models that were considered had values of β of 0.1, 0.2 and 0.4. The range of β was chosen to approximate complete redistribution of angular momentum (uniform rotation) to local conservation of angular momentum during stellar evolution except in the convective core. The properties of the models selected are tabulated in Table 3.1. These models were chosen to keep the surface equatorial radius nearly the same for possible comparison of oscillation frequencies. Figure 3.2 presents a plot of the meridional plane to illustrate the difference in shape
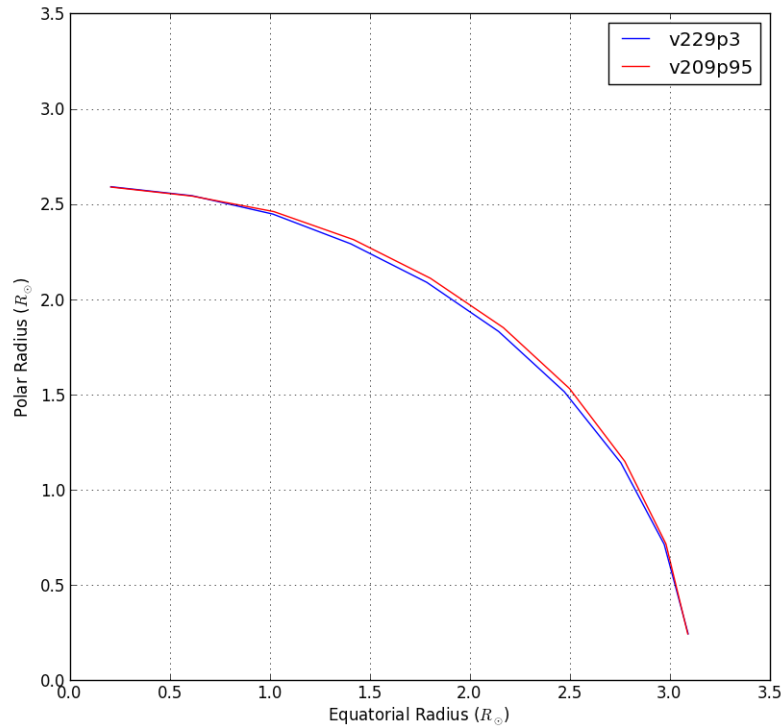
Figure 3.2: Cross section of the selected uniform rotating model (Blue curve) and the highest differentially rotating model with $\beta = 0.4$ (Red curve).

between the uniform rotating model, V229p3, and the most differentially rotating model, V209p95. Clearly, the changes in the surface structure are relatively modest.

3.2   Results

Figure 3.3 compares the SEDs of the four rotating models with the observations in the UV and visible regions. Both the synthetic data and the measured data were filtered with a boxcar filter of 50Å of bandwidth and the distance of 14.6pc has been used to obtain the CLIC fluxes.

All four models agree fairly well when compared with the observations, similar to the

Table 3.1
Properties of models considered

Model ID	V_{eq} (km s^{-1})	Mass ($M_\odot$)	Luminosity ($L_\odot$)	T_{eq} (K)	R_{eq} ($R_\odot$)	R_{pole}/R_{eq}	T_{pole}/T_{eq}	β
V229p3	229.3	2.1975	32.58	7570.	3.101	0.838	1.176	0
V224	224.	2.20	32.60	7571.	3.101	0.838	1.179	0.1
V219	219.	2.05	32.54	7569.	3.102	0.838	1.184	0.2
V209p95	209.95	2.11	32.38	7569.	3.099	0.838	1.196	0.4

result we obtained for V236_Xc25 (Deupree et al. (2012)). From the figure it is clear that it is difficult to detect sizeable differences between the uniform model and the others which have different angular momentum distributions in their interior. Enlarged views of the UV and the visible regions are shown on Figure 3.4a and 3.4b respectively. A quantitative test was done to compare how well the rotational models fit the data compared to the spherical model that best fit the observations (a non-rotating CLIC computed model with $T_{eff} = $ 7875K). To quantify the comparison in the ultraviolet, we computed the the difference between the observed flux and the computed fluxes every sampled point in the IUE dataset from $1174\mathring{A} - 1878\mathring{A}$ and every 10Å for the IUE dataset from $1900\mathring{A} - 3200\mathring{A}$ and then calculated the standard deviation for these differences for each of the two IUE data sets. The $10\mathring{A}$ sampling of the second IUE dataset produces more than a hundred points to include in the calculation and is comparable to the sampling in the far UV dataset. To make the comparison in the visual part of the spectrum the magnitude of the difference in the fluxes was computed every 25Å, which was the digitization frequency of the observed data. The four rotating models are all close to each other, so for the sake of the comparison with the spherical counterpart, only V229p3 was used.

The fit to the data in the visible is about the same as that of the 7875 K effective temperature model; they agree to within 1%. In the UV the standard deviation of the difference between the observations and the rotating model was five times smaller compared to the 7875 K model for the far-ultraviolet data set ($1174\mathring{A} - 1878\mathring{A}$), although comparison of Figures 3.3 and 3.4 show that neither fits the SED perfectly. Each model is identified by its β parameter, characterizing the amount of differential rotation included. We note that the far-ultraviolet data set does not have the prominent peak at about $1600\mathring{A}$ that all rotating models and the spherical model possess. This plays a role in the far-ultraviolet error comparison, making no model particularly good in the shortest wavelengths of this spectral region. For the second IUE ultraviolet data set ($1900\mathring{A} - 3200\mathring{A}$), the rotating model SED still fits better than the spherical model, having an average difference 35% smaller. Although this better agreement with the observations for the rotating model SED provides some validation both for the rotating models themselves and of the numerical approach of integrating the localized surface temperatures and gravities over the surface to obtain the observed flux, the uncertainty associated with these IUE observations hinders the possibility to pick one model as best-fit.

Figure 3.4a does show some differences among the SEDs for the different rotating models, but they are so small that hardly any conclusion can be drawn about the actual internal angular momentum distribution of α Oph from just the SED, at least from the range chosen.

In light of the small differences between the rotating models and even the spherical case considered, something that one might ask is how much does every latitudinal zone contribute to the flux at each wavelength and how does it change with the inclination at
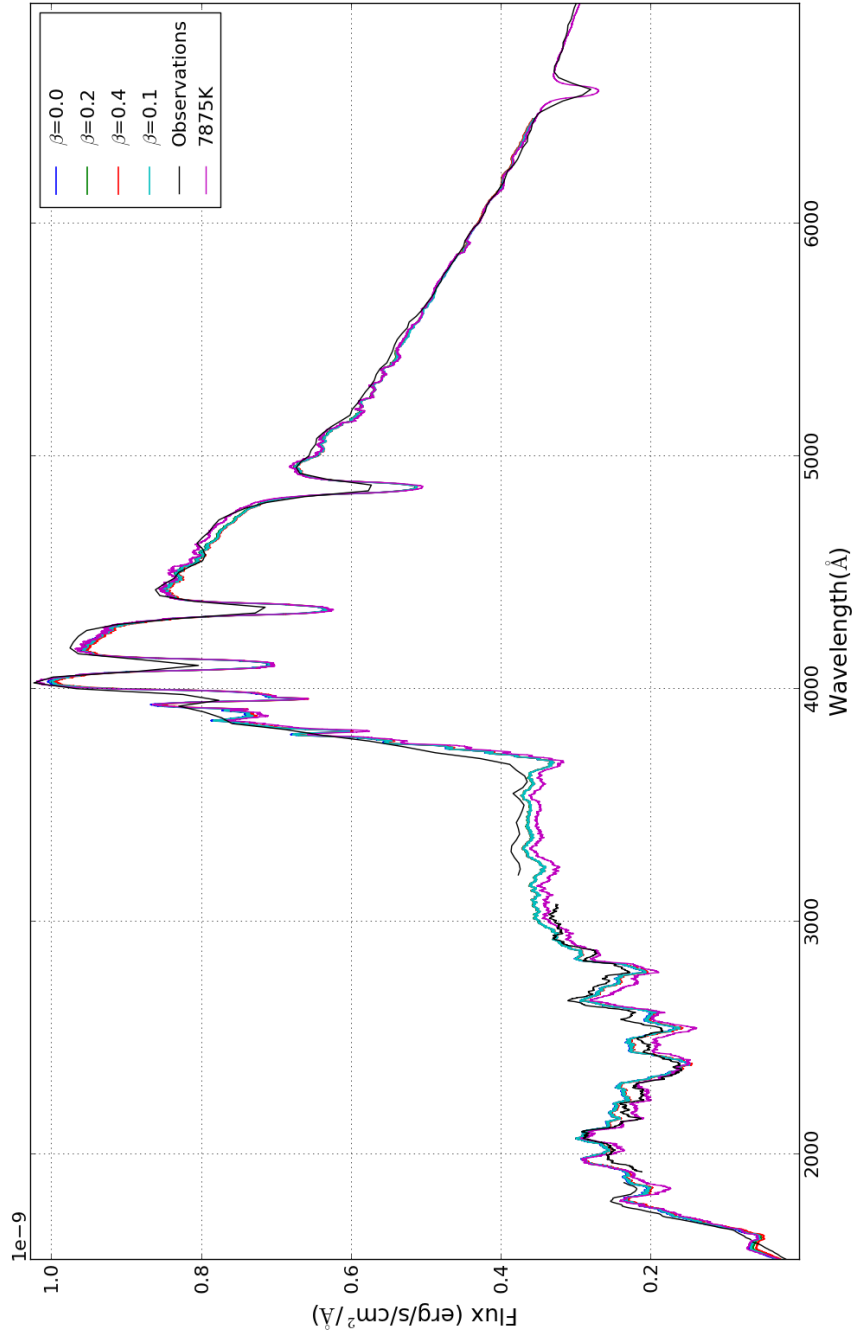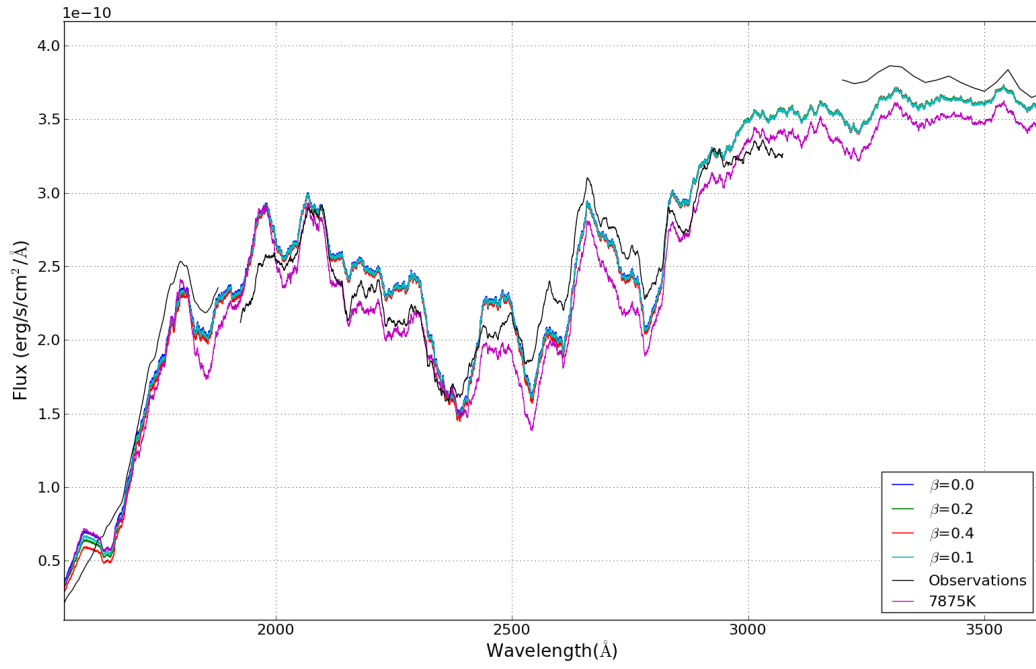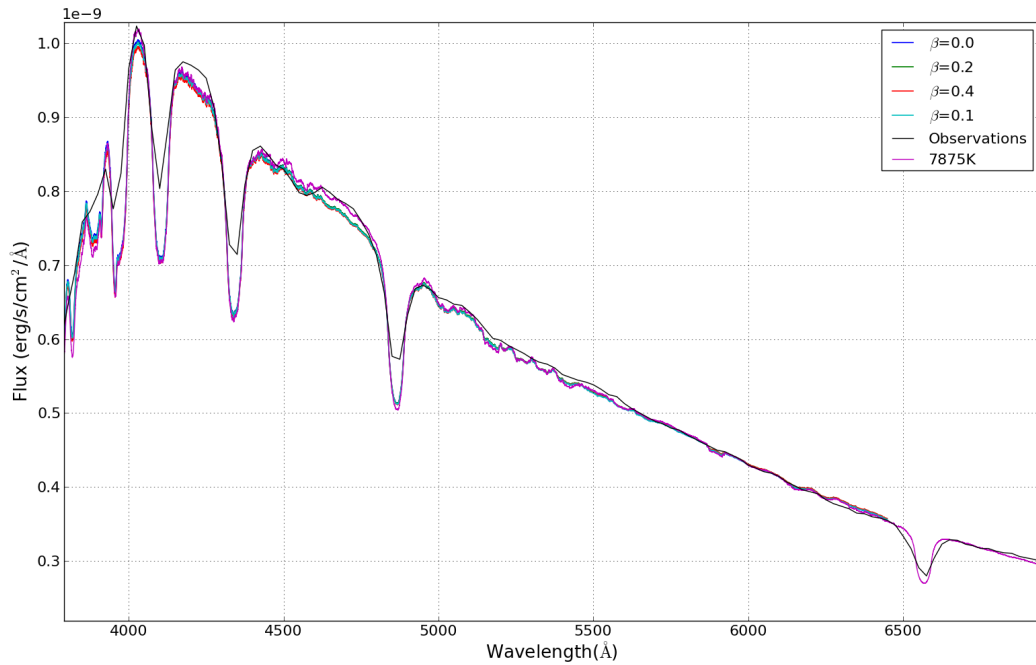
Figure 3.3: Model suite vs. observation data

(a)

(b)

Figure 3.4: UV and visible enlargements of the synthetic SEDs and the observations

which the star is being observed. In the case of α Oph, which is observed almost equator-on, we performed a test by calculating a SED in which the flux contribution of the poles was excluded. We omitted from the integration colatitudinal zones from $0° - 30°$ and $150° - 180°$, and then we found the percentage of the flux that would be missing in the observed spectra as a function of wavelength. Figure 3.5 shows the result of this calculation as a function of inclination. From this ratio it was unexpectedly found that when observed equator-on, the exclusion of the pole only takes away around 2.5% of the total flux except in the far ultraviolet, where the models do not do a particularly good job in reproducing the (comparatively small) flux. This just shows that the hottest zone of the star's surface is almost irrelevant in terms of flux contribution. A second test omitting the contribution of all zones with latitudes higher than 30% (Figure 3.6) shows that the regions surrounding the equator, in which temperatures vary from $\sim 7900K - 7570K$, contribute more than 70% of the total flux for α Oph, again with the exception of the far ultraviolet. This also indicates why the spherical model with constant surface temperature that best fit the observations has a $T_{eff} = 7875K$. This analysis also points out that fast rotators for which the deduced inclination lies around $40°$ may be very interesting to study. Figure 3.5 shows that around this inclination one would expect all latitudinal zones to be contributing importantly to the total flux, both requiring the kind of modeling approach used in this work and perhaps providing the best inclination for being able to study the effects of rotation on the SED.

In the next chapter we will extend the study of the different selected models by including calculations of individual lines, including the Doppler broadening for comparison with the observed line profiles.
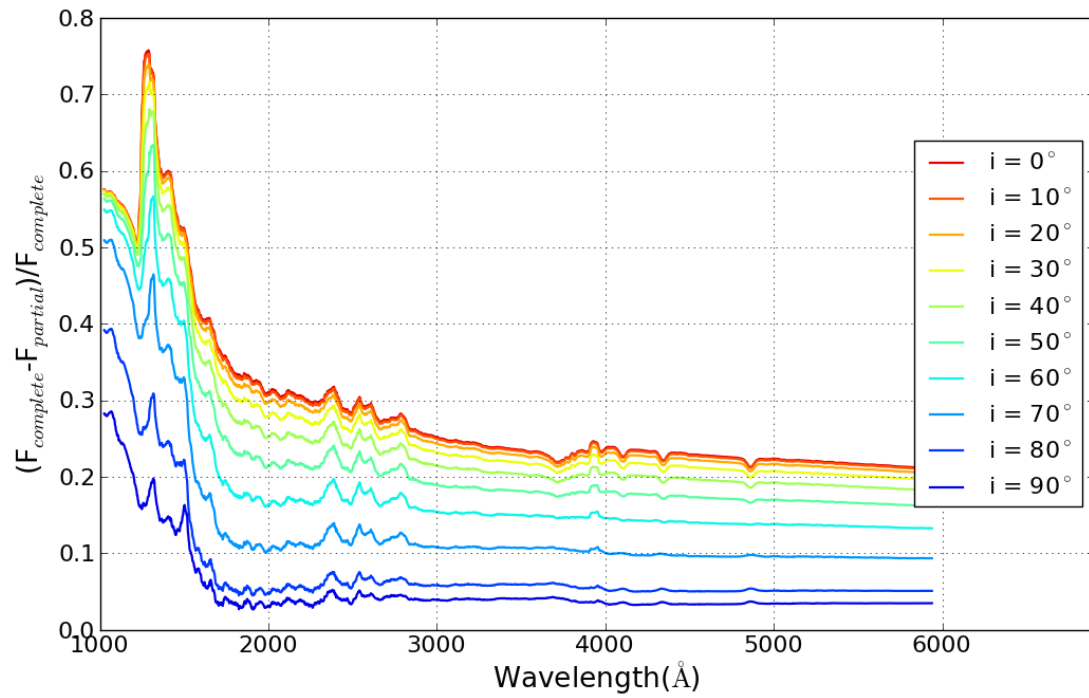
Figure 3.5: Percentage of flux lost from the V229p3 model when the polar region is excluded from the calculation. We set the polar region to be between $0° - 30°$, and $150° - 180°$ in latitude.
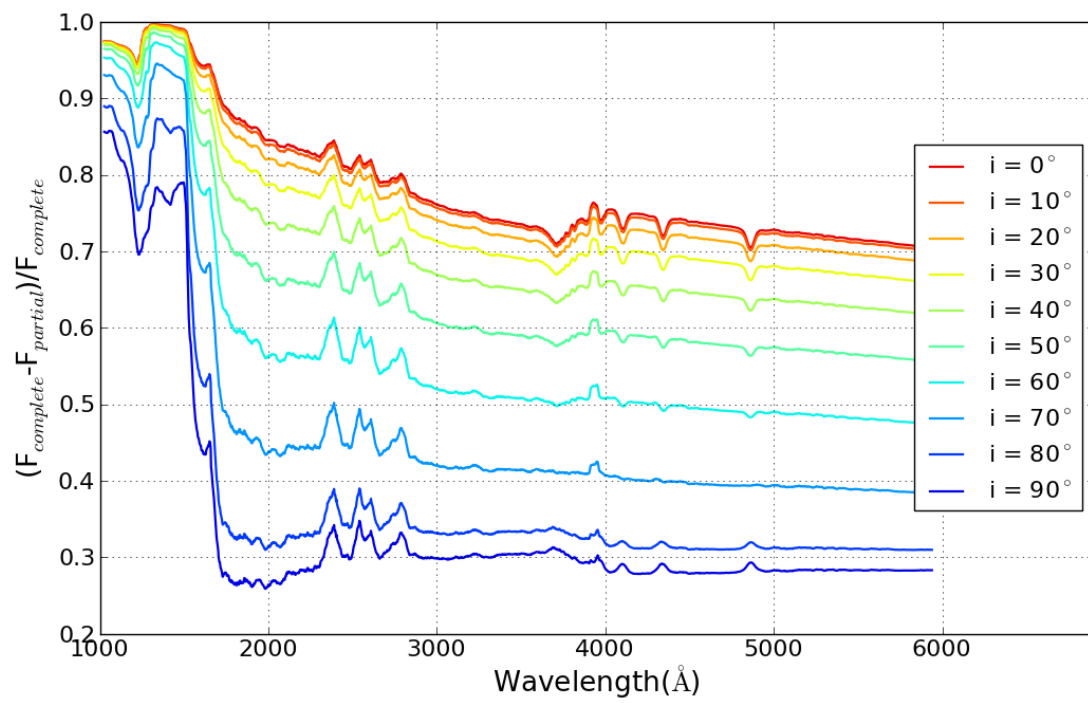
Figure 3.6: Percentage of flux subtracted from the V229p3 model when a region of 60° from the pole is excluded from the CLIC integration.

Chapter 4

Lines

It was effectively impossible to determine which rotation law fits what we observe from α Oph better by comparing only the full SED because the difference were so small. However, it is conceivable that studying individual spectral lines could provide a better discriminant of the rotation law. We thus used the same set of models as in the SED analysis to look at differences in several line profiles between these models and the observations of α Oph. Potentially, these comparison plots could identify a model with a certain internal angular momentum distribution as the best fit.

CLIC has the ability to synthesize individual spectral lines including all rotational effects. There is no need to invoke any limb or gravity darkening law because the atmospheric and internal model construction of the star provide the necessary data to calculate the real effect in the line profile. Unlike SED calculations, in "line mode" CLIC includes the Doppler effect of rotation as well. We began by searching for prominent lines in the observed ultraviolet and visual spectra of α Oph. Once a line was selected, PHOENIX

provided the identification of every absorption feature, including the element name and ionization stage. With all this information however, the identification of lines (particularly in the UV part of the spectra) became a challenge. As expected, iron dominated most of the SED absorption features between 1500 and 3000Å, with most lines being blended. Five lines were selected in this wavelength range by visual inspection for comparison with the IUE observations. The selection was based on their absorption strength and how many elements were responsible for each one of them. We wanted to study lines that were produced only by one element, hence containing only the Doppler broadening in their profile, but this proved to be almost impossible with the exception of three cases in the UV, a FeII line at $2599\text{\AA}$ and the Mg H/K lines at $2799\text{\AA}$ and $2801\text{\AA}$. The rest of the line features selected have various elements as responsible members of the absorption. A summarized list with all the spectral lines considered is given in Table 4.1 and the corresponding comparison plots are shown in Figures 4.1 to 4.5. As in the study of the SED, we included the observed spectrum and the spectra computed for the models in Table 3.1. We have also calculated with CLIC the line profiles of the best fit spherical model of $T_{eff} = 7875\text{K}$ assuming the rotational velocities of the uniform rotating model to include the Doppler broadening effect. This was the only rotational effect included in the spherical model.

From the complete SED analysis we know that the continuum for our models does not perfectly match the averaged IUE continuum, but here what we wish to focus on is how the different angular momentum distributions would affect the line profiles themselves and how they will compare with the observations. With this in mind, for each line we matched the continuum surrounding the line by multiplying the computed flux by a constant. This
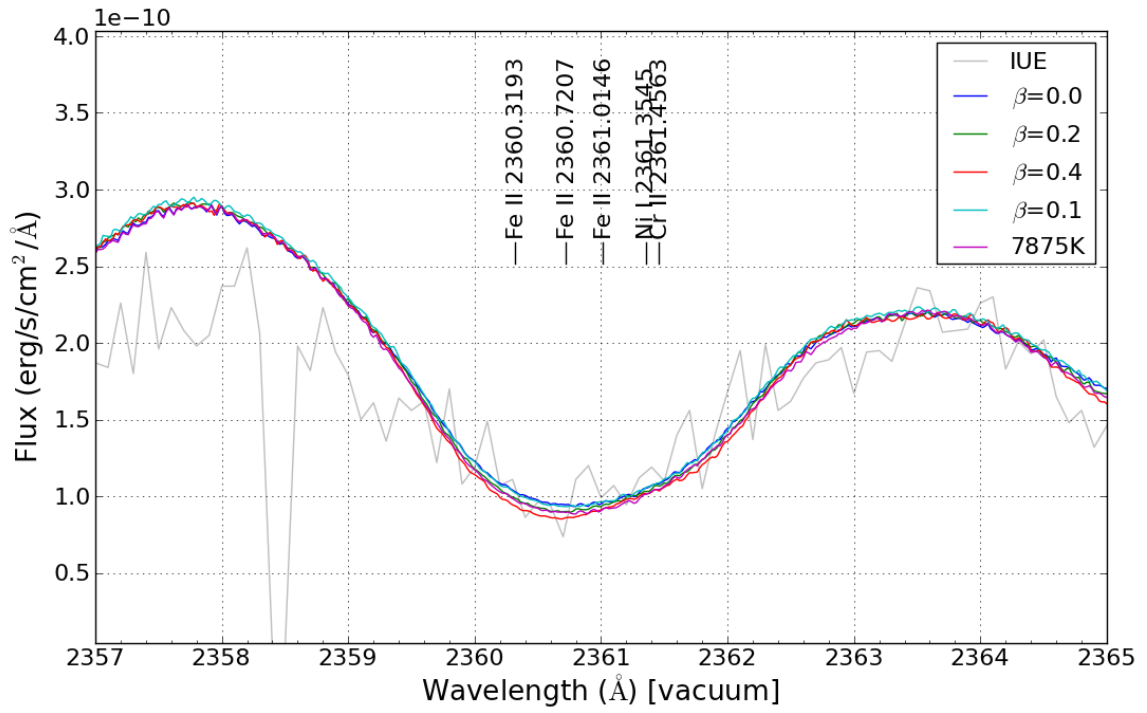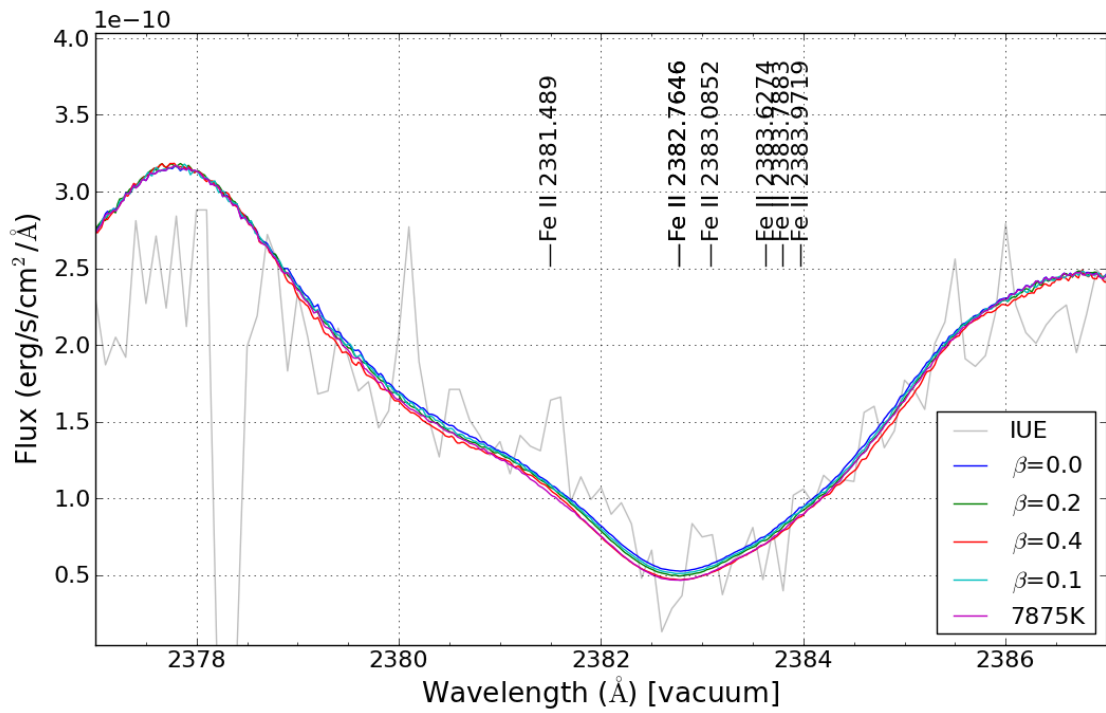
Figure 4.1: Line features surrounding $2360\mathring{A}$

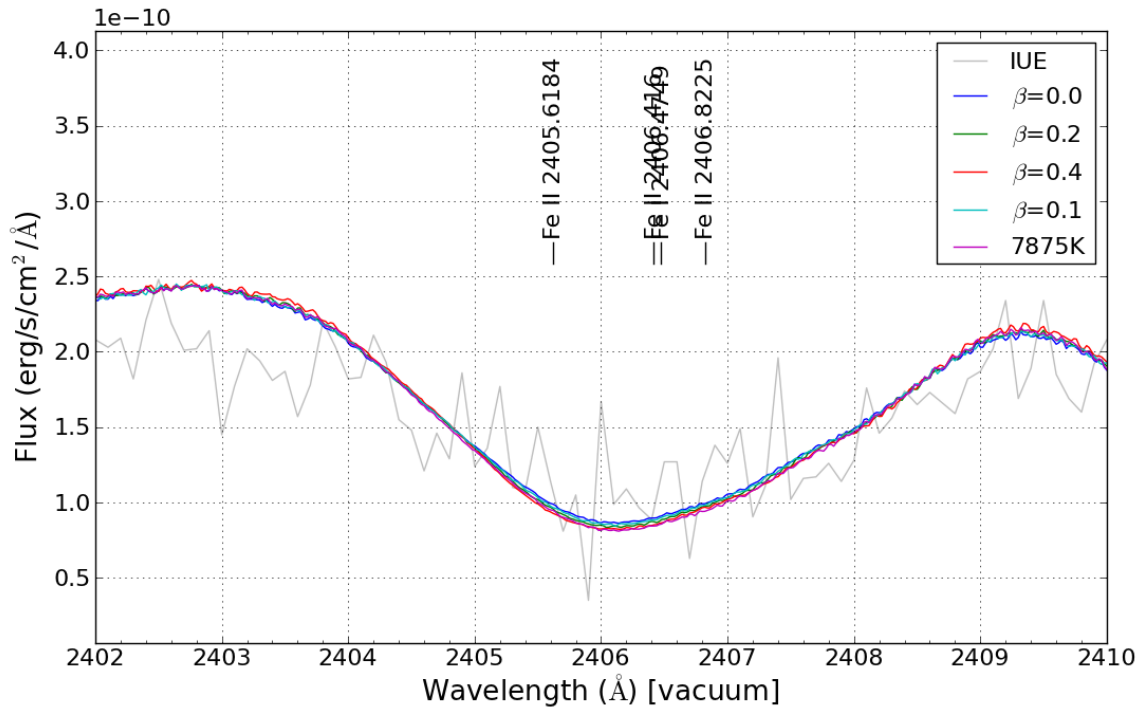Figure 4.2: Line features surrounding $2382\mathring{A}$

Figure 4.3: Line features surrounding 2406Å
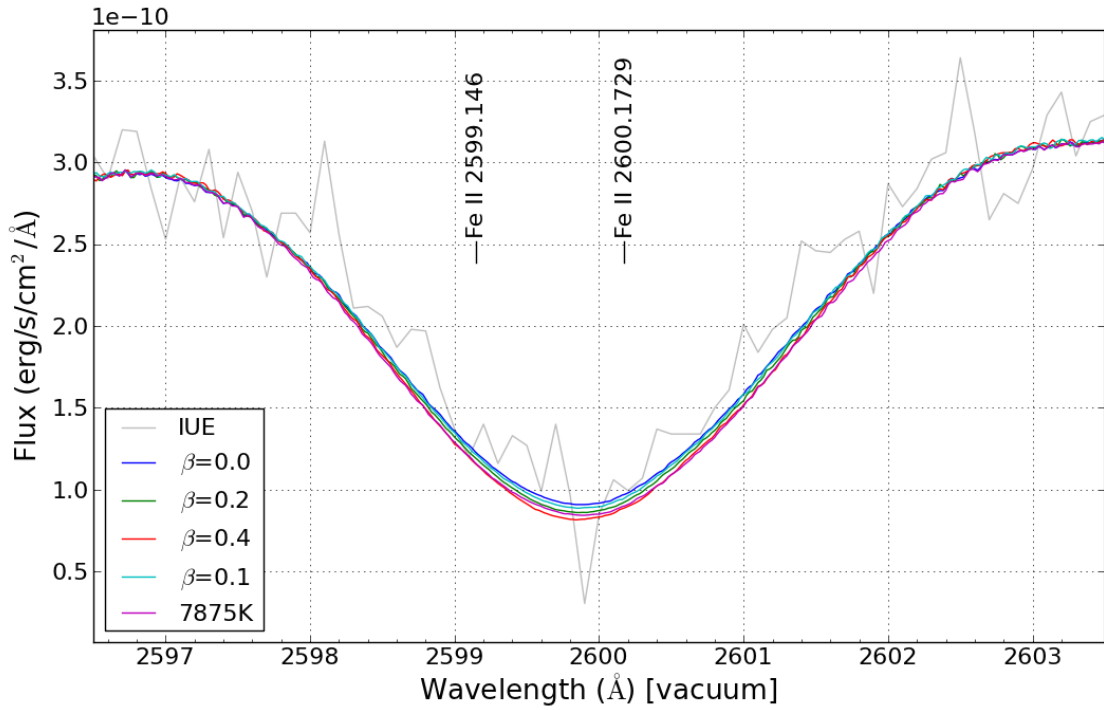

Figure 4.4: Line at 2599Å

Table 4.1
Properties of ultraviolet lines considered

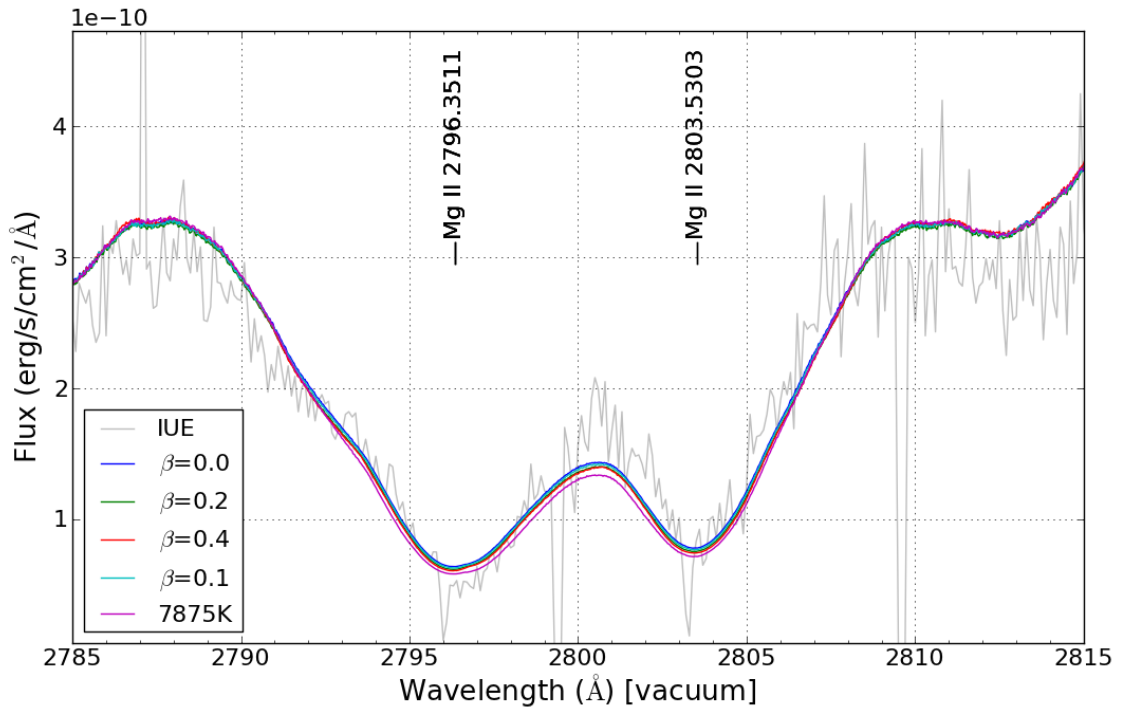| Ion	Wavelength (Å) [in vacuum]	Figure #
Fe II	2360.3193, 2360.7207, 2361.0146	
Ni I	2361.3545	4.1
Cr II	2361.4563	
Fe II	2381.489, 2382.7646, 2383.0852, 2383.6274 2383.7883, 2383.9719	4.2
Fe II	2405.6184, 2406.416, 2406.4749	4.3
Fe I	2406.8225	
Fe II	2599.146, 2600.1729	4.4
Mg H/K II	2796.3511, 2803.5303	4.5

Figure 4.5: Final UV selected line: Mg H/K

Table 4.2
Properties of visual lines considered

Ion	Wavelength (Å) [in vacuum]	Figure #
Ca II	3934.7773	4.6
Sr II	4216.7061	4.7
Fe I	4218.7329, 4226.644, 4228.6162	
Ca I	4227.9185	
Cr II	4617.9219, 4620.0872	4.8
Fe II	4621.814	
Cr I	5205.9556, 5207.4862, 5209.8691	4.9
Fe I	5216.6333, 5217.7266	
Ti II	5227.997	
Fe I	5228.3158, 5228.6455, 5234.3975, 5236.8452	4.10
Fe II	5236.0806	
Cr II	5238.7856	

constant factor was around ~ 0.9 in the worst cases.

Figures 4.1 - 4.5 show good agreement among all the models and the IUE observations. The differences in the line profiles among the models are so small, however, that it is not possible to say which model fits better. The spherical model also seems to match each line well, as might be expected from the latitudinal flux contribution analysis performed at the end of the last chapter.

At visual wavelengths a similar approach was used, but here we compared these lines with a high resolution spectra made available by Allende Prieto et al. (2004). This data set was composed of a spectrum with a resolution $R \simeq 50\,000$ and was only useful for the line analysis because it had the continuum removed. For the comparison, our computed CLIC SED was normalized using a local slope calculated from the observed values in both far wings of each line. The lines considered are summarized in Table 4.2 and the results shown in Figures 4.6 - 4.9.
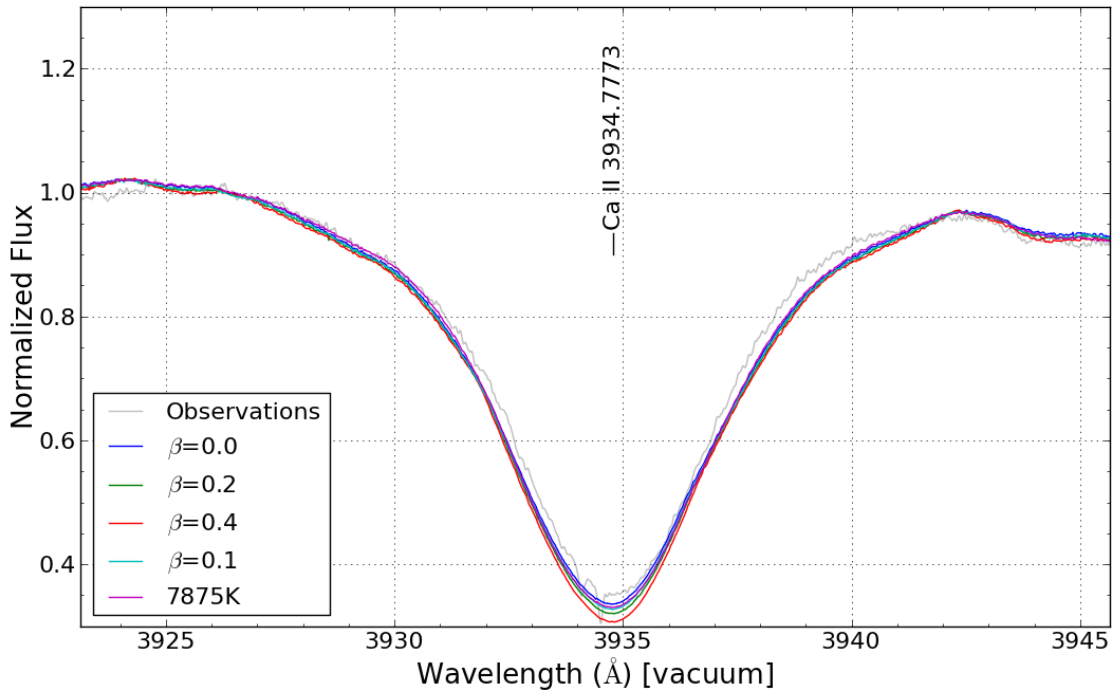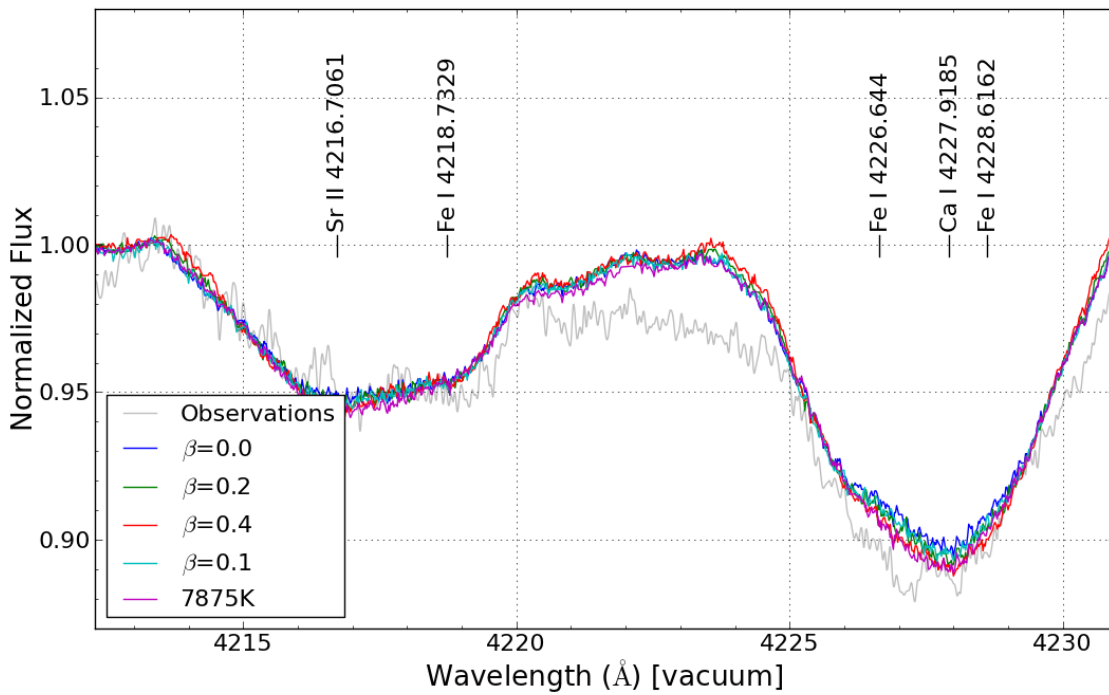
Figure 4.6: CaII line at $3934\mathring{A}$

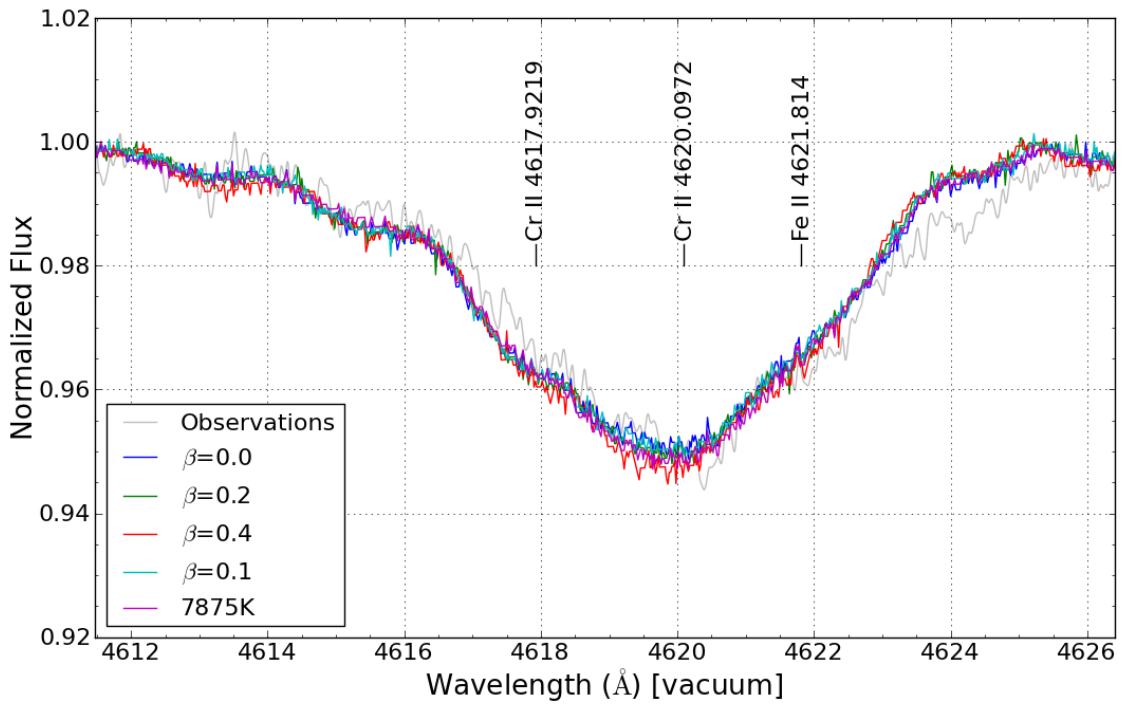Figure 4.7: Line features in the range between $4212\mathring{A} - 4232\mathring{A}$

Figure 4.8: Line features surrounding 4620Å
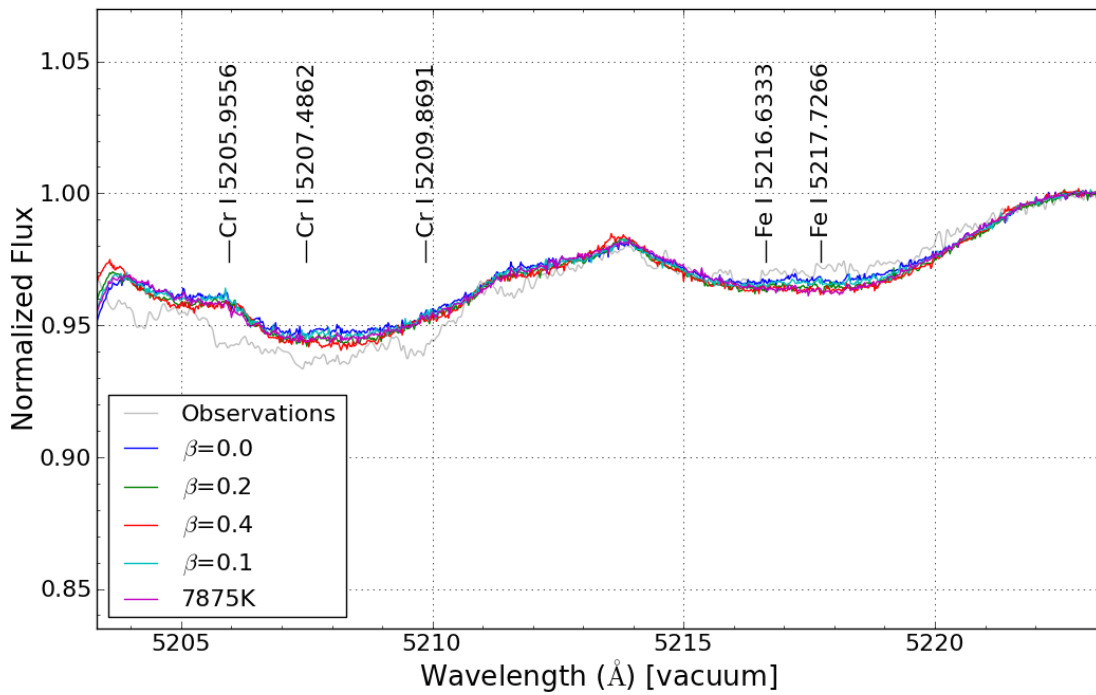
Figure 4.9: Line features between $5203\text{Å} - 5223\text{Å}$
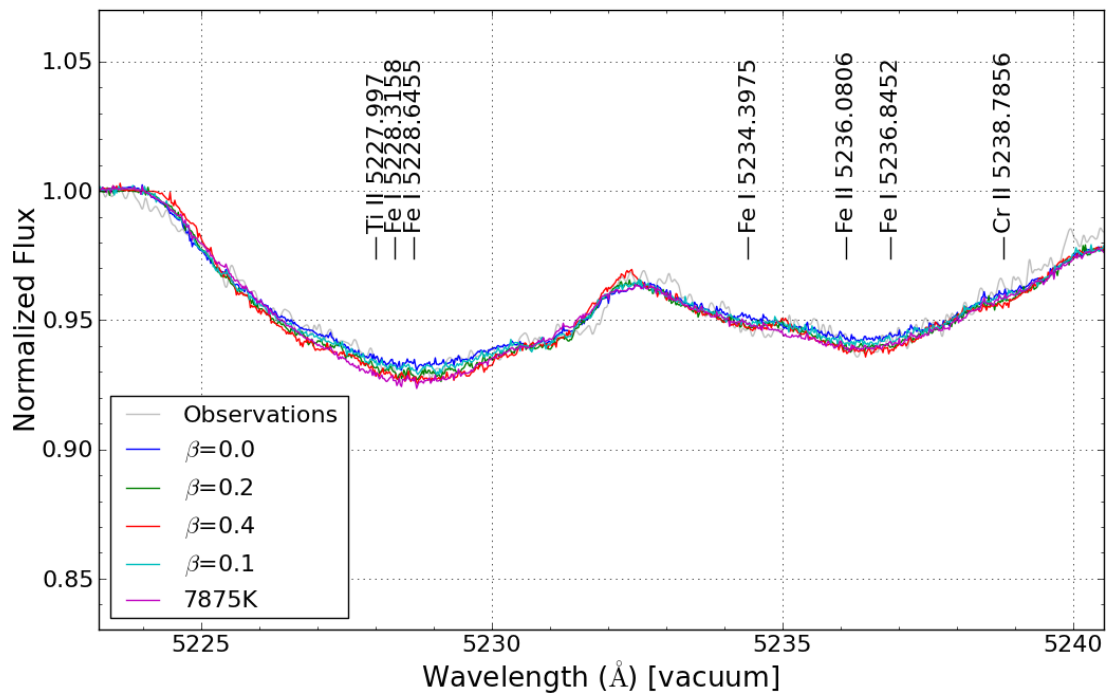
Figure 4.10: Line features between $5223\text{Å} - 5240\text{Å}$

The plots show that the agreement between line profiles in the models and the observations continues in the visible. Small differences can be seen in some cases (e.g. Figure 4.9). For this particular case it is unlikely that that problem is in the iron abundance because we match other iron lines rather well (e.g. Figure 4.4).

We have tried to address all aspects of making the model SEDs as realistic as possible and appear to have been rewarded with a reasonably good fit to the line profile data. It is of some interest to see how much the results would change by reducing the level realism in the modeling by assuming that the atmospheric models are in LTE. To compare the results we calculated LTE versions of the PHOENIX models and then we analyzed the resultant line profiles for the specific lines used above. Figures 4.11 and 4.12 show an example case of this comparison. The first plot shows the Ca II line produced by the spherical model of $T_{eff} = 7875$K without including rotation effects, to point out the differences between the NLTE and LTE model line profiles. Clearly a number of lines show some differences in the amount of absorption in the core of the line. The picture looks somewhat different when the rotational broadening is included (Figure 4.12). Rotation in this case blends away most differences, with some small deviations from one to another in the far end of the wings and in the core of the line. For these differences to be relevant when comparing the profiles to an observed SED, one must have very low uncertainties for the flux measurements. Although it is a good practice to include as much realism into the modeling of the star as possible, for the specific geometry and surface properties of the α Oph case, the NLTE and LTE considerations do not appear to play a big role in determining a better matching model at least for the specific lines examined here.
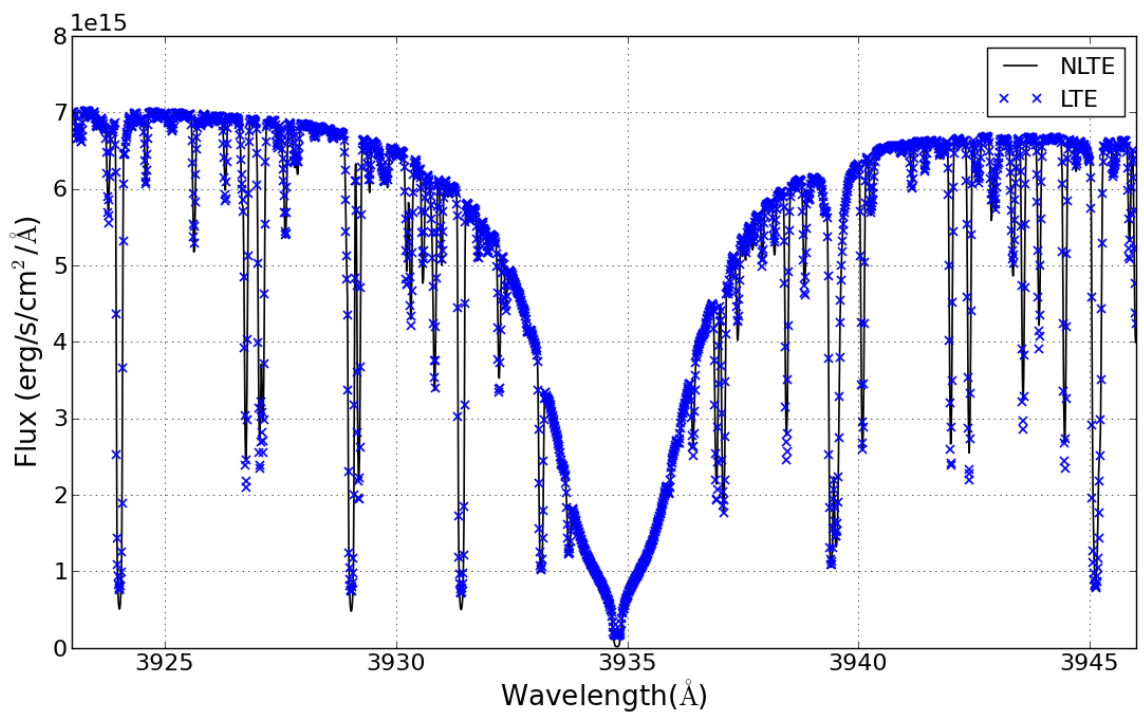
Figure 4.11: Line profile comparison between the best-fit spherical atmospheric model in NLTE and the model in LTE. The lines have not been rotationally broadened.
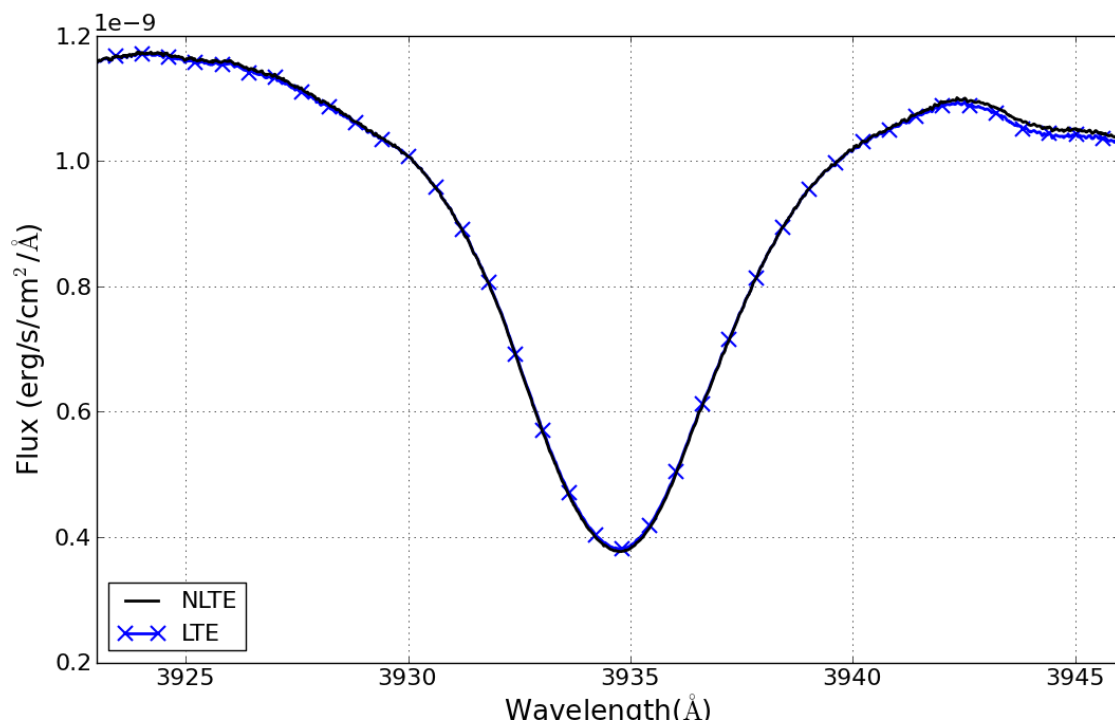
Figure 4.12: Broadened line profile comparison between the best-fit spherical atmospheric model in NLTE and the nodel in LTE

Chapter 5

Conclusions

The goal of this work was to compare the SEDs and absorption line profiles of theoretical stellar models that included slightly different internal angular momentum distributions with the observed SED and line profiles of the rapidly rotating, δ Scuti star, α Oph. This star is an interesting case for study because many of its surface properties (inclination, oblateness, temperature difference between pole and equator) have been deduced through interferometry, so the degrees of freedom in the stellar model generation are greatly reduced. The asteroseismic observations make α Oph a good test probe of detailed models of rotating stars.

We have already presented a first attempt of matching the SED with a uniformly rotating model (Deupree et al. 2012), achieving a good fit to observations. This fit was also better than that of a spherical model with the deduced effective temperature of the star. However, one would expect for a star as evolved as α Oph (expected to be in relatively late core hydrogen burning) that uniform rotation is not the most likely rotation law. While there is no

reason to believe that the rotation law remains conservative because the stellar core proba-
bly rotates somewhat more rapidly than the outer layers, we have approximated plausible
rotation rates by three conservative differentially rotating models in which the material
closer to the polar axis rotates more rapidly than the material farther away. All models
matched the interferometric oblateness, although the surface shapes at mid latitudes were
slightly different. The non-LTE stellar atmosphere and spectrum synthesis code PHOENIX
was used to generate a grid of plane-parallel stellar atmospheres which covered the full
range of effective temperature and effective gravity values at all latitudes for all the mod-
els of α Oph. Finally, the intensity integrator code CLIC was used to calculate SEDs and
absorption line profiles from the ROTORC models for comparison with available observa-
tions of α Oph. One of the advantages of the procedure followed here is that there is no
need to include any limb or gravity darkening law into account because the atmospheric
and internal model construction of the star provide the necessary data to calculate the real
effect on the SED and line profile.

We selected a well-exposed pair of IUE spectra and also an OAO2 dataset that covered
the ultraviolet spectrum from 1150Å to 3200Å. The IUE had good resolution but a fairly
high standard deviation for each flux measurement, while the OAO2 had a small standard
deviation but a relatively low resolution. After filtering the IUE data with a 50$\mathring{A}$ wide
boxcar filter, both agree within uncertainties in some, but not all, wavelength regions, but
it is not possible to select one as better than the other without having more observations.
We chose to compare our results with the higher resolved IUE data set to be able to compare
the line profiles. We were able to fit the observed SEDs fairly well with our model SEDs in

both the UV and the visual, and the line profile fits to the data were generally quite good.

The SED comparison showed that the four selected ROTORC models with different internal angular momentum distributions produce SEDs which are very close to each other, and it is very hard to distinguish any one model from the others. Each of the four models provide a reasonable fit to the observed SEDs in both the ultraviolet and visual parts of the spectrum. They also show that for a star that is differentially rotating following equation 2.1 with values of $\beta = 0.1 - 0.4$, it is almost impossible to say which model resembles more closely the real internal rotational profile of α Oph. We also found that by observing the star equator-on, most of the flux contribution comes from latitudes around the equator even though the equatorial region is noticeably cooler than the higher latitudes. An exclusion of a $30°$ latitude zone around the pole removes only $\sim 2.5\%$ of the total flux for all wavelength regions studied except those in the far ultraviolet where the total flux is comparatively small. This analysis shows that a very interesting case to study would be a rapidly rotating star observed to be inclined at around $40°$, a configuration in which the visible surface of both the pole and the equator would play an important role in the observed SED.

We extended the analysis of the same set of models by considering individual line profiles. The selection of each line was done by visual inspection of both the synthetic SEDs and the observations. We looked for prominent features that if possible were composed of just one element. The PHOENIX code provided the identification of each line. Vertical scaling was required in some of the models because the observed and modeled continua were not always perfectly matched, as was seen in the SED comparison for all the models with respect to the observations. The scaling factor departed from unity by about 10% in

the worst cases. After the continuum was adjusted, the lines calculated with CLIC agreed well with the observational data and, once again, the differences between each model in the suite were too small to definitely point to a single model as the one which provided the best fit.

It is thus difficult to determine a best-fit β parameter just from the calculated SED and individual lines for these low differential rotation regimes. One last test for this suite of models, beyond the scope of this work, would be to consider their oscillation properties and how well they compare with the MOST data for α Oph. This might shed light on a preferred model that describes better the possible internal configuration on the star.

A interesting future case of study would be the historically important photometric standard star, Vega, which was discovered to be rapidly rotating from the anomalous flat-bottomed appearance of many of its weak metal lines, which could only be explained by model of a star seen nearly pole-on ($i \sim 5°$) and rotating at around 245 km/s at the equator (Gulliver et al. 1991, 1994). More recently, Aufdenberg et al. (2006) studied Vega interferometrically with the CHARA array and found values of $i = 4.7° \pm 0.3°$ and an equatorial velocity of (270 ± 15)km/s by fitting rotating models that included gravity darkening approximations. We could potentially provide a better constraint on the properties of Vega by applying the method followed in this work for α Oph, with the advantage that in Vega's case the amount of observational data available is quite large and of better quality. Thought to have an inclination of $\sim 57°$, Altair presents another interesting case (Monnier et al. 2007). For this inclination, both the polar and equatorial regions would be expected to contribute significantly to the flux. Such a case might provide a better test of both the rotating

models and the approach used. van Belle (2012) presents a catalog of 354 new possible rapid rotating targets that can be resolved interferometrically with current instrumentation, suggesting that there will be many opportunities to apply our method and maybe help understand the physics of the interior of rotating stars.

Bibliography

Abt, H. A., Levato, H., & Grosso, M. 2002, The Astrophysical Journal, 573, 359

Abt, H. A. & Morrell, N. I. 1995, The Astrophysical Journal Supplement Series, 99, 135

Allen, C. W. 1973, Astrophysical Quantities, 3rd edn.

Allende Prieto, C., Barklem, P. S., Lambert, D. L., & Cunha, K. 2004, Astronomy and Astro-physics, 420, 183

Aufdenberg, J. P., Merand, A., du Foresto, V. C., et al. 2006, The Astrophysical Journal, 645, 664

Bautista, M. A., Romano, P., & Pradhan, A. K. 1998, The Astrophysical Journal Supplement Series, 118, 259

Bernacca, P. L. & Perinotto, M. 1970, Contr. Oss. Astrof. Padova in Asiago

Blackwell, D. E. & Lynas-Gray, A. E. 1998, Astronomy and Astrophysics Supplement Series, 129, 505

Bodenheimer, P. 1971, The Astrophysical Journal, 167, 153

Breger, M. 2000, Delta Scuti and Related Stars, 210

Burnashev, V. 1985, Abastumanskaya Astrofiz. Obs. Bull., 59

Carciofi, A. C., Domiciano de Souza, A., Magalhães, A. M., Bjorkman, J. E., & Vakili, F. 2008, The Astrophysical Journal, 676, L41

Carroll, J. A. 1928, Monthly Notices of the Royal Astronomical Society, 88, 548

Carroll, J. A. 1933, Monthly Notices of the Royal Astronomical Society, 93, 478

Che, X., Monnier, J. D., Zhao, M., et al. 2011, The Astrophysical Journal, 732, 68

Claret, A. 2003, Astronomy and Astrophysics, 406, 623

Clement, M. J. 1974, The Astrophysical Journal, 194, 709

Clement, M. J. 1978, The Astrophysical Journal, 222, 967

Clement, M. J. 1979, The Astrophysical Journal, 230, 230

Code, A. D. & Meade, M. R. 1979, The Astrophysical Journal Supplement Series, 39, 195

Collins, G. W. 1963, The Astrophysical Journal, 138, 1134

Collins, G. W. & Truax, R. J. 1995, The Astrophysical Journal, 439, 860

Collins, G. W., Truax, R. J., & Cranmer, S. R. 1991, The Astrophysical Journal Supplement Series, 77, 541

Crawford, I. 2001, Monthly Notices of the Royal Astronomical Society, 327, 841

Demarque, P., Guenther, D. B., Li, L. H., Mazumdar, A., & Straka, C. W. 2007, Astrophysics and Space Science, 316, 31

Deupree, R. G. 1990, The Astrophysical Journal, 357, 175

Deupree, R. G. 1995, The Astrophysical Journal, 439, 357

Deupree, R. G. 1998, The Astrophysical Journal, 499, 340

Deupree, R. G. 2011, The Astrophysical Journal, 742, 9

Deupree, R. G., Castañeda, D., Peña, F., & Short, C. I. 2012, The Astrophysical Journal, 753, 20

Domiciano de Souza, A., Kervella, P., Jankov, S., et al. 2003, Astronomy and Astrophysics, 407, L47

Drawin, H. W. 1961, Zeitschrift fur Physik, 164, 513

Eggenberger, P., Meynet, G., Maeder, A., et al. 2007, Astrophysics and Space Science, 316, 43

Endal, A. S. & Sofia, S. 1976, The Astrophysical Journal, 210, 184

Endal, A. S. & Sofia, S. 1978, The Astrophysical Journal, 220, 279

Erspamer, D. & North, P. 2003, Astronomy and Astrophysics, 398, 1121

Espinosa Lara, F. 2010, Astrophysics and Space Science, 328, 291

Faulkner, J., Roxburgh, I. W., & Strittmatter, P. A. 1968, The Astrophysical Journal, 151, 203

Frémat, Y., Zorec, J., Hubert, A.-M., & Floquet, M. 2005, Astronomy and Astrophysics, 440, 305

Gatewood, G. 2005, The Astronomical Journal, 130, 809

Gillich, A. 2007, Master's Thesis, Saint Mary's University, Halifax, Nova Scotia

Gillich, A., Deupree, R. G., Lovekin, C. C., Short, C. I., & Toqué, N. 2008, The Astrophysical Journal, 683, 441

Gray, R. O., Graham, P. W., & Hoyt, S. R. 2001, The Astronomical Journal, 121, 2159

Gulliver, A. F., Adelman, S. J., Cowley, C. R., & Fletcher, J. M. 1991, The Astrophysical Journal, 380, 223

Gulliver, A. F., Hill, G., & Adelman, S. J. 1994, The Astrophysical Journal, 429, L81

Hauschildt, P. H. & Baron, E. 1999, J. Comput. Appl. Math., 109

Hinkley, S., Monnier, J. D., Oppenheimer, B. R., et al. 2011, The Astrophysical Journal, 726, 104

Jackson, S. 1970, The Astrophysical Journal, 161, 579

Jackson, S., MacGregor, K. B., & Skumanich, A. 2004, The Astrophysical Journal, 606, 1196

Jackson, S., MacGregor, K. B., & Skumanich, A. 2005, The Astrophysical Journal Supplement Series, 156, 245

Johnson, H. L. & Harris, D. L. 1954, The Astrophysical Journal, 120, 196

Johnson, H. L. & Knuckles, C. F. 1957, The Astrophysical Journal, 126, 113

Johnson, H. L., Mitchell, R. I., Iriarte, B., & Wisniewski, W. Z. 1966, Communications of the Lunar and Planetary Laboratory, 4

Kanaan, S., Meilland, A., Stee, P., et al. 2008, Astronomy and Astrophysics, 486, 785

Kervella, P., Domiciano de Souza, A., Kanaan, S., et al. 2009, Astronomy and Astrophysics, 493, L53

Kippenhahn, R. 1977, Astronomy and Astrophysics, 58, 267

Kippenhahn, R., Meyer-Hofmeister, E., & Thomas, H. C. 1970, Astronomy and Astrophysics, 5

Kippenhahn, R. & Thomas, H. 1970, Stellar Rotation

Kurucz, R. 1994, Atomic Data for Fe and Ni (Cambridge: SAO)

Kurucz, R. L. & Bell, B. 1995, Atomic Line List (Cambridge: SAO)

Linnell, A. P. & Hubeny, I. 1994, The Astrophysical Journal, 434, 738

Lovekin, C. 2005, Master's Thesis, Saint Mary's University, Halifax, Nova Scotia

Lovekin, C. C., Deupree, R. G., & Short, C. I. 2006, The Astrophysical Journal, 643, 460

Lucy, L. B. 1967, Zeitschrift für Astrophysik, 65

MacGregor, K. B., Jackson, S., Skumanich, A., & Metcalfe, T. S. 2007, The Astrophysical Journal, 663, 560

Maeder, A. 1999, Astronomy and Astrophysics, 347, 185

Maeder, A. & Peytremann, E. 1970, Astronomy and Astrophysics, 7, 120

Malagnini, M. L. & Morossi, C. 1990, Astronomy and Astrophysics Supplement Series (ISSN 0365-0138), 85, 1015

Mathisen, R. 1984, Photo Cross Sections for Stellar Atmosphere Calculations: Compilation of References and Data (Oslo: Univ. Oslo)

McAlister, H. A., ten Brummelaar, T. A., Gies, D. R., et al. 2005, The Astrophysical Journal, 628, 439

Monaghan, F. F. & Roxburgh, I. W. 1965, Monthly Notices of the Royal Astronomical Society, 131

Monnier, J. D., Townsend, R. H. D., Che, X., et al. 2010, The Astrophysical Journal, 725, 1192

Monnier, J. D., Zhao, M., Pedretti, E., et al. 2007, Science (New York, N.Y.), 317, 342

Ostriker, J. P. & Mark, J. W.-K. 1968, The Astrophysical Journal, 151, 1075

Paturel, G., Petit, C., Prugniel, P., et al. 2003, Astronomy and Astrophysics, 412, 45

Reilman, R. F. & Manson, S. T. 1979, The Astrophysical Journal Supplement Series, 40, 815

Reiners, A. 2003, Astronomy and Astrophysics, 408, 707

Roxburgh, I. W., Griffith, J. S., & Sweet, P. A. 1965, Zeitschrift für Astrophysik, 61

Royer, F., Grenier, S., Baylac, M.-O., Gï¿œmez, A. E., & Zorec, J. 2002, Astronomy and Astrophysics, 393, 897

Sackmann, I.-J. & Anand, S. P. S. 1970, The Astrophysical Journal, 162, 105

Seaton, M. J., Yan, Y., Mihalas, D., & Pradhan, A. K. 1994, Monthly Notices of the Royal Astronomical Society, 266

Shajn, G. & Struve, O. 1929, Monthly Notices of the Royal Astronomical Society, 89, 222

Short, C. I., Hauschildt, P. H., & Baron, E. 1999, The Astrophysical Journal, 525, 375

Slettebak, A. 1949, The Astrophysical Journal, 110, 498

Slettebak, A., Kuzma, T. J., & Collins, G. W. 1980, The Astrophysical Journal, 242, 171

Townsend, R. H. D., Owocki, S. P., & Howarth, I. D. 2004, Monthly Notices of the Royal Astronomical Society, 350, 189

Uesuga, A. & Fukuda, I. 1970, MnKyo, 33, 205

van Belle, G. T. 2012, The Astronomy and Astrophysics Review, 20, 51

van Belle, G. T., Ciardi, D. R., Thompson, R. R., Akeson, R. L., & Lada, E. A. 2001, The Astrophysical Journal, 559, 1155

Vinicius, M. M. F., Zorec, J., Leister, N. V., & Levenhagen, R. S. 2006, Astronomy and Astrophysics, 446, 643

von Zeipel, H. 1924, Monthly Notices of the Royal Astronomical Society, 84, 665

Xu, Y., Li, Z.-P., Deng, L.-C., & Xiong, D.-R. 2002, Chinese Journal of Astronomy &
Astrophysics, 2, 441

Zhao, M., Monnier, J. D., Pedretti, E., et al. 2009, The Astrophysical Journal, 701, 209